CM² MAGAZINE

第 66 期

南方科技大学海洋磁学中心主编

https://cm2.sustech.edu.cn/

创刊词

海洋是生命的摇篮，是文明的纽带。地球上最早的生命诞生于海洋，海洋里的生命最终进化成了人类，人类的文化融合又通过海洋得以实现。人因海而兴。

人类对海洋的探索从未停止。从远古时代美丽的神话传说，到麦哲伦的全球航行，再到现代对大洋的科学钻探计划，海洋逐渐从人类敬畏崇拜幻想的精神寄托演变成可以开发利用与科学研究的客观存在。其中，上个世纪与太空探索同步发展的大洋科学钻探计划将人类对海洋的认知推向了崭新的纬度：深海（deep sea）与深时（deep time）。大洋钻探计划让人类知道，奔流不息的大海之下，埋藏的却是亿万年的地球历史。它们记录了地球板块的运动，从而使板块构造学说得到证实；它们记录了地球环境的演变，从而让古海洋学方兴未艾。

在探索海洋的悠久历史中，从大航海时代的导航，到大洋钻探计划中不可或缺的磁性地层学，磁学发挥了不可替代的作用。这不是偶然，因为从微观到宏观，磁性是最基本的物理属性之一，可以说，万物皆有磁性。基于课题组的学科背景和对海洋的理解，我们对海洋的探索以磁学为主要手段，海洋磁学中心因此而生。

海洋磁学中心，简称 CM^2，一为其全名“Centre for Marine Magnetism”的缩写，另者恰与爱因斯坦著名的质能方程 $E = MC^2$ 对称，借以表达我们对科学巨匠的敬仰和对科学的不懈追求。

然而科学从来不是单打独斗的产物。我们以磁学为研究海洋的主攻利器，但绝不仅限于磁学。凡与磁学相关的领域均是我们关注的重点。为了跟踪反映国内外地球科学特别是与磁学有关的地球科学领域的最新研究进展，海洋磁学中心特地主办 CM^2 Magazine，以期与各位地球科学工作者相互交流学习、合作共进！

“海洋孕育了生命，联通了世界，促进了发展”。 21 世纪是海洋科学的时代，由陆向海，让我们携手迈进中国海洋科学的黄金时代。

目 录

1. 在末次冰期-间冰期转换过程中莫桑比克边缘海的早期成岩过程的演化 1

2. 汇聚边缘构造过程对生物圈和地质圈的影响和反馈 7

3. 堆晶橄榄石：重稀土元素成矿的新宿主 13

4. 北大西洋冰川东部边界流对冰盖-AMOC 相互作用和气候变化的重要驱动作用 16

5. 下加利福尼亚(28-30°N) San Borja 和 Jaraguay 单成因火山群的综合古地磁研究:有关纬度校正 23

6. 东亚热带地区在过去 60ka 的季节性干旱事件 27

7. 南海东部次海盆海底扩张过程中洋壳结构和岩浆作用随时间的变化 30

8. 中国直升机时域电磁技术进展 33

9. 始新世以来夏威夷岛链飘移的新证据 35

10. 在空间变化的岩浆流中晶体的旋转和排列 38

11. 非洲东南部 2500 cal BP 以来的古地磁记录.....42

12. 太平洋深水冲刷和冰消期大气 CO_2 浓度的上升.....45

1. 在末次冰期-间冰期转换过程中莫桑比克边缘海的早期成岩过程的演化

翻译人：仲义 zhongy@sustech.edu.cn

Zindorf M, Rooze J, Meile C, et al. ***The evolution of early diagenetic processes at the Mozambique margin during the last glacial-interglacial transition [J]****. Geochimica et Cosmochimica Acta, 2021, 300, 79-94.*

https://doi.org/10.1016/j.gca.2021.02.024

摘要: 莫桑比克边缘海经历着巨大的沉积速率的变化，主要是由于在末次冰期-全新世过渡时期来自赞比西河流的沉积物改道作用。沉积物堆积和有机质埋藏对沉积物中自生矿物的形成具有重要的控制作用，这些矿物的分布可以反映古环境和古气候的演化历史。结合孔隙水和沉积物的地球化学分析和输运模拟的方法，作者重建了莫桑比克边缘海地区过去 27 千年以来沉积历史及其对黄铁矿形成和生物地球化学过程的变化。拟合模型匹配上观测到的地球化学模式显示，最重要的自生黄铁矿可以重建过去硫酸盐-甲烷过渡带的深度变化，其深度迁移响应者沉积物堆积和有机质沉积的变化。沉积物沉积的迅速变化影响了有机碎屑硫酸盐还原和伴生的黄铁矿的形成，但对厌氧甲烷氧化和随后的黄铁矿形成的影响滞后了几千年。模型结果揭示了从末次冰期高成岩反应速率的近岸环境向现今低反应速率的离岸环境转化的过程。值得注意的是，在硫酸盐-甲烷过渡带及其以下的成岩过程中，过去产生的甲烷残留物和溶解铁质油藏仍然在形成。由于全球大陆边缘都发生了冰架泛洪和相应的沉积环境变化，本文分析的非稳态成岩作用在大陆边缘沉积物中的响应，并对沉积物输入变化较大的沉积物岩心进行古海洋解释具有重要作用。

ABSTRACT: The Mozambique continental margin experienced large variations in sedimentation rates, primarily due to re-routing of sediment deposition from the Zambezi River during the last glacial-Holocene transition. As changes in sediment accumulation and organic matter deposition impose a strong control on the formation

of authigenic minerals in the sediment, the distribution of these minerals may reflect the regional paleoenvironmental and paleoclimatic evolution. Combining geochemical analyses of porewaters and sediments with a reactive transport modeling approach, we reconstruct the depositional history and its effect on pyrite formation and other biogeochemical transformations at a site on the Mozambique margin over the past 27 kyr. Fitting the model to match the observed geochemical patterns, most importantly authigenic pyrite, allowed for the reconstruction of past sulfate-methane transition zone depth, which migrated in response to changes in the sediment accumulation and organic matter deposition. Changes in sediment deposition quickly affected organoclastic sulfate reduction and associated pyrite formation, but the effect on anaerobic methane oxidation and subsequent pyrite formation occurred with a lag on the order of thousands of years. Model results reveal a transition from high diagenetic reaction rates representative of near-shore depositional environments during the late glacial maximum, to a setting typical of offshore sediments with low reaction rates at the present day. Notably, the remnants of methane and dissolved iron pools produced in the past still shape the diagenetic processes at and below the sulfate-methane transition zone today. Since deglacial shelf-flooding and corresponding changes in sediment deposition occurred along continental margins worldwide, our analysis highlights the important role of non-steady state diagenesis in continental margin sediments and its relevance for paleoceanographic interpretation of sediment cores experiencing strong variations in sediment input.

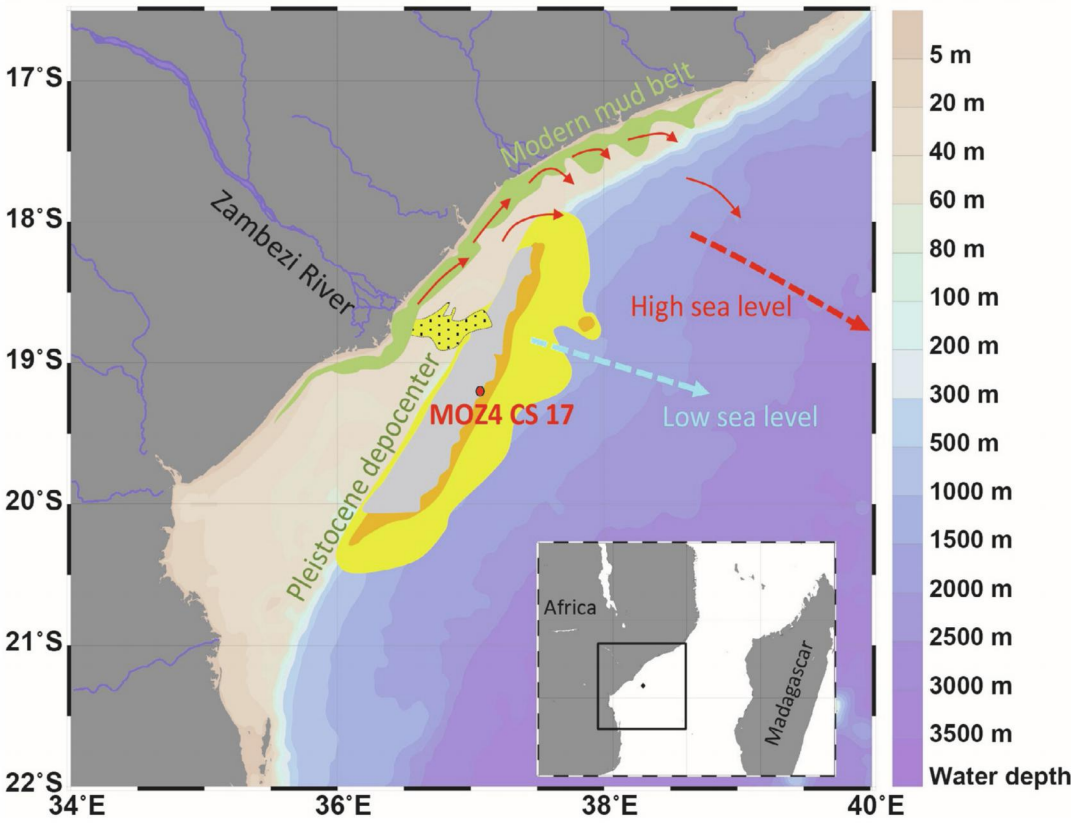

Fig1. Map of the area of investigation. Red dot indicates position of Site MOZ4-CS17; arrows indicate direction of sediment transport during Pleistocene low sea-level (light blue); and during modern high sea-level (red) (Schulz et al., 2011); Thickness (increasing from yellow = 0–400 m to orange = 400–800 m to gray > 800 m shaded areas) of Pleistocene lowstand sediment deposition center centers inferred from the seismic investigations (Walford et al., 2005); modern sediment deposition (green mud-belt interpreted by van der Lubbe et al., 2014); Paleo-Zambezi incised valley (yellow dotted area; Walford et al., 2005). The 100 m isobath approximately indicates dry shelf area during Pleistocene sea-level lowstand 20 kyr BP (brown hues). Bathymetric map created with Ocean Data View (Schlitzer, 2015). (For interpretation of the references to color in this figure legend, the reader is referred to the web version of this article.)

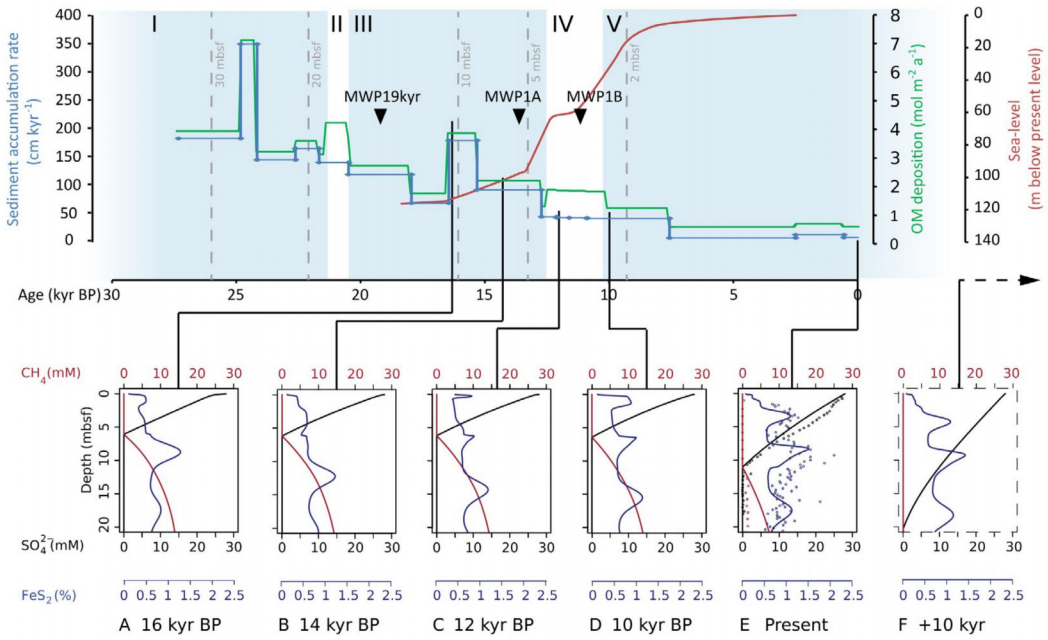

Fig2. a) Temporal evolution of modeled profiles (in small plots A-F) of sulfate (black), methane (red) and pyrite (blue) in response to sediment accumulation rate (blue), OM deposition (green) and paleo-sea-level (red; Camoin et al., 2004) in the upper plot. Roman numerals indicate phases of OM deposition (see Table 3). Blue shaded background indicates phases of normal OM deposition; white shaded phases indicate phases of increased OM deposition. Gray stippled vertical lines indicate corresponding depth in sediment core MOZ4-CS17. (For interpretation of the references to color in this figure legend, the reader is referred to the web version of this article.)

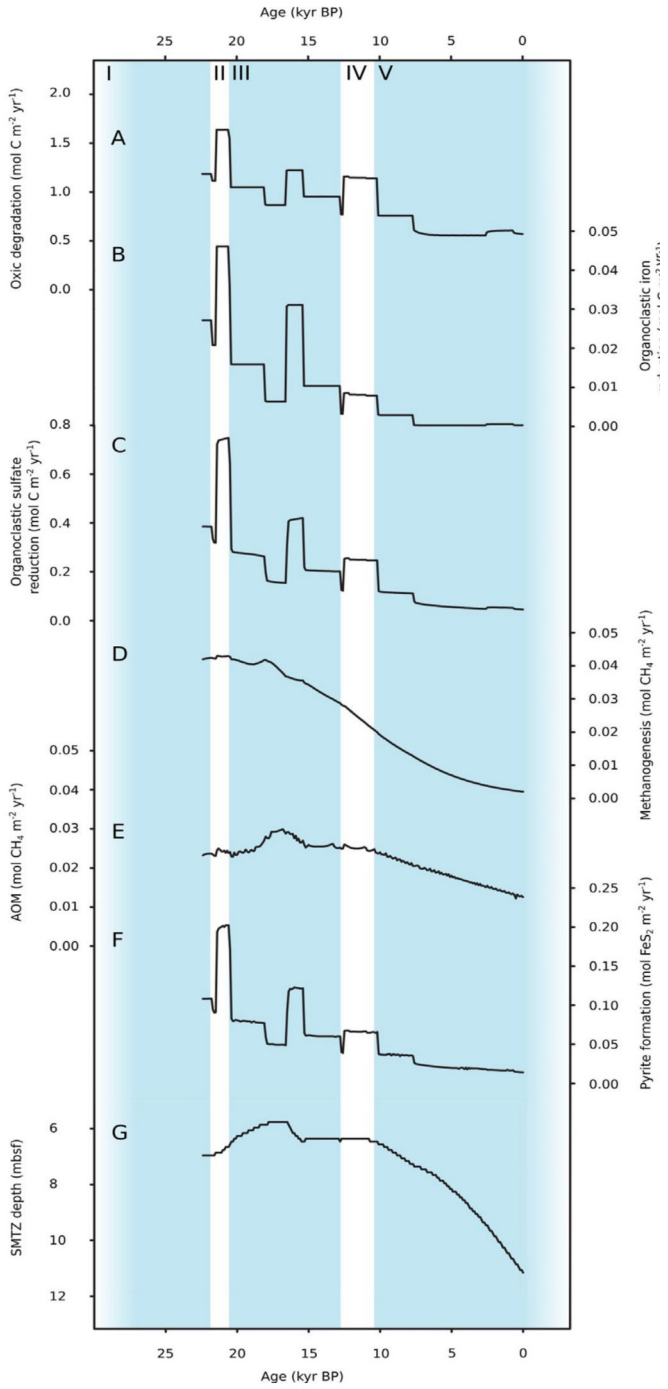

Fig3. Depth-integrated reaction rates over time. (A) Oxic degradation, (B) organoclastic iron reduction, (C) organoclastic sulfate reduction, (D) methanogenesis, (E) anaerobic oxidation of methane, (F) pyrite formation, (G) sulfate-methane transition zone depth (note reversed y-axis). Periods of increased OM deposition are indicated by white background as in Fig. 3.

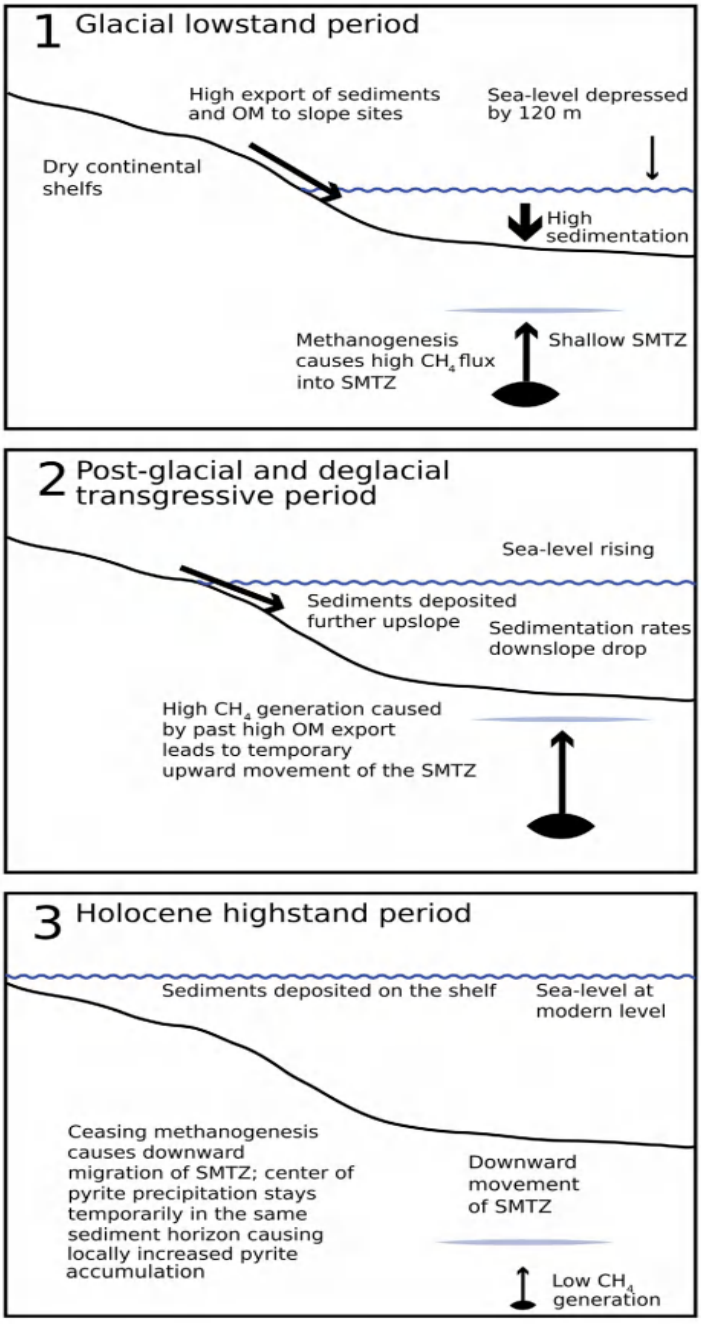

Fig4. Schematic illustration for diagenetic evolution at the Mozambique margin (not to scale). Panels 1–3 correspond to the three-step conceptual model discussed in the text

2. 汇聚边缘构造过程对生物圈和地质圈的影响和反馈

翻译人：蒋晓东 jiangxd@sustech.edu.cn

Fullerton K M, Schrenk M O, Yücel M, et al. ***Effect of tectonic processes on biosphere-geosphere feedbacks across a convergent margin [J]****. Nature Geoscience, 2021, online*

https://doi.org/10.1038/s41561-021-00725-0

摘要：地下岩石圈蕴含了地球上最大的生物量，但是板块边界和俯冲地质过程的微生物群落的变化程度仍然不清楚。本文对哥斯达黎加汇聚边缘 21 个热泉中微生物群落和深度岩石圈的地球化学性质进行比较。发现热泉阳离子和阴离子反应了下部构造结构的倾角，并且对应于微生物群落变化。同时出现了与培养型化能无机自养型微生物相关的群落，这些菌落能够利用反转三羧酸循环，此外反转三羧酸循环元基因组的丰度与板片挥发性碳的浓度相关。这些结果联合碳同位素证据，表明俯冲板片来源的二氧化碳进入生物系统很可能支持了基于化能无机自养的地下生物圈。我们估算这种弧前地下生物圈每年能够固碳 1.4×10^9 到 1.4×10^{10} 摩尔。这可能会使地幔传输总碳估算降低 2%到 22%。基于本研究发现的相关性，我们认为地下岩石圈细菌群落的分布与组成很可能受到哥斯达黎加聚敛边缘深部构造过程的影响，并且隔绝俯冲过程的碳挥发。这些化能自养微生物群落也能反过来影响地质圈层。

ABSTRACT: The subsurface is among Earth's largest biomes, but the extent to which microbial communities vary across tectonic plate boundaries or interact with subduction-scale geological processes remains unknown. Here we compare bacterial community composition with deep-subsurface geochemistry from 21 hot springs across the Costa Rican convergent margin. We find that cation and anion compositions of the springs reflect the dip angle and position of the underlying tectonic structure and also correlate with the bacterial community. Co-occurring microbial cliques related to cultured chemolithoautotrophs that use the reverse tricarboxylic acid cycle (rTCA) as well as abundances of metagenomic rTCA genes correlate with concentrations of slab-

volatilized carbon. This, combined with carbon isotope evidence, suggests that fixation of slab-derived CO_2 into biomass may support a chemolithoautotrophy-based subsurface ecosystem. We calculate that this forearc subsurface biosphere could sequester 1.4×10^9 to 1.4×10^{10} mol of carbon per year, which would decrease estimates of the total carbon delivered to the mantle by 2 to 22%. Based on the observed correlations, we suggest that distribution and composition of the subsurface bacterial community are probably affected by deep tectonic processes across the Costa Rican convergent margin and that, by sequestering carbon volatilized during subduction, these chemolithoautotrophic communities could in turn impact the geosphere.

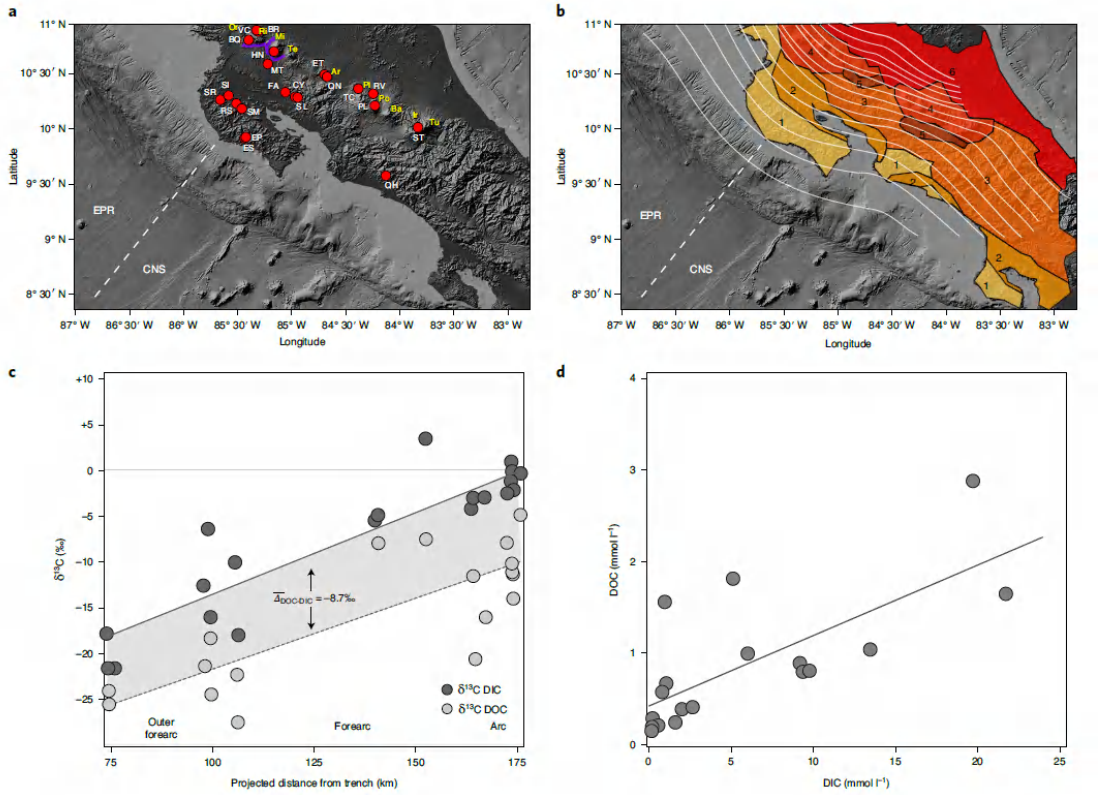

Fig1. Sites span the Costa Rican convergent margin, with organic matter produced from chemolithoautotrophy of deep-slab inorganic carbon. **a**, Locations of the sampled hot springs and volcanic crater lake (red markers with white labels), volcanoes (yellow labels) and the calderas of the Guanacaste Geothermal Province (purple lines, adapted from Tassi et al.38). **b**, Subducting slab depth lines (thin lines every 10 km depth, thick lines every 50 km depth) and principal bedrock types: (1) Cretaceous/Tertiary ophiolites; (2) Tertiary basins; (3) Tertiary volcanic range; (4) Quaternary volcanic range; (5) intra-arc basins; (6) Caribbean coastal plain (adapted from Tassi et al.39). Dotted lines show the boundary between the plates of the EPR and CNS. **c**, $\delta^{13}C$ values of DIC and DOC show similar spatial trends with the projected distance from the trench (solid and dashed lines with R2 values of 0.81 and 0.65 for DIC and DOC, respectively) with an average offset (Δ DOC−DIC) of $-8.7 \pm 1.3‰$. d, Concentrations of DOC and DIC correlate with each other (Pearson moment correlation $R^2 = 0.53$, $P < 0.01$, $n = 18$) across the sampled sites (site SL is off the scale with 5.69 mmol l^{-1} DIC and 6.29 mmol l^{-1} DOC). Data in c and d were used in previously published calcite precipitation models[16].

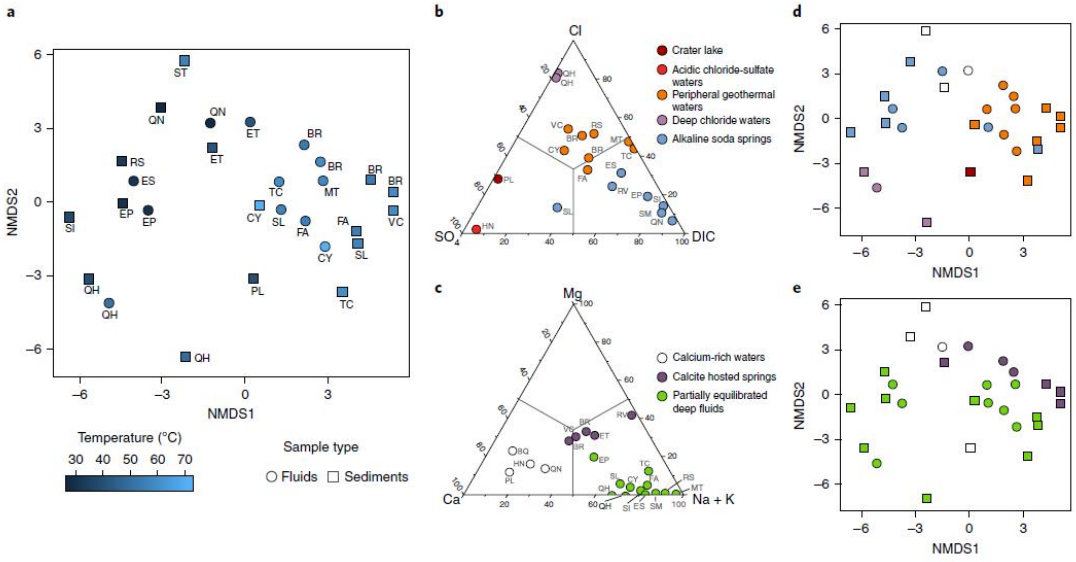

Fig 2. Clustering of the sites based on microbial community diversity and geochemical characteristics. **a**, NMDS (stress 0.17) plot of the 16S rRNA gene amplicon microbial diversity based on Jaccard dissimilarity measure in the fluids (circles) and sediments (squares), coloured by spring temperature, with sample names corresponding to those of Fig. 1. **b**, **c**, Ternary diagrams showing the clustering of the samples based on the major anions (b) and major cations (c). **d**, **e**, The same NMDS plot from a, but coloured according to the geochemistry-based grouping from b (anions, ADONIS $P < 0.05$, $n = 19$, Holm-corrected) and c (cations, ADONIS $P < 0.05$, $n = 21$, Holm-corrected), respectively. Empty symbols in d and e represent samples for which one or more ions were missing, and therefore have no placement in **b** and **c**.

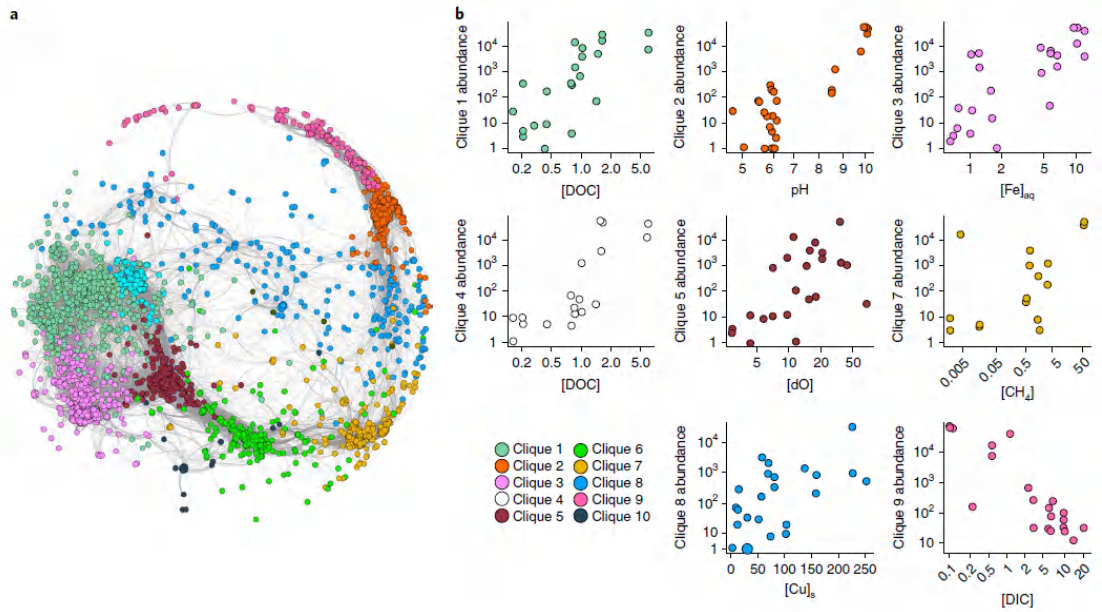

Fig 3. Bacterial cliques each have different relationships to subduction zone geochemistry. **a**, Co-occurrence network analysis of the dominant ASVs across all sampling sites, coloured by clique, with positive Spearman correlations >0.7 plotted as edges. **b**, Sum of ASVs in each clique plotted against the subduction zone geochemical variable identified by RF, Spearman correlation and Pearson correlation as the major explanatory variable for that clique ($P < 0.01$, Holm-corrected, $n = 16 - 25$). Cliques 6 and 10 were not significantly correlated with any geochemical variable. Concentrations are indicated by square bracket notation. dO, dissolved oxygen.

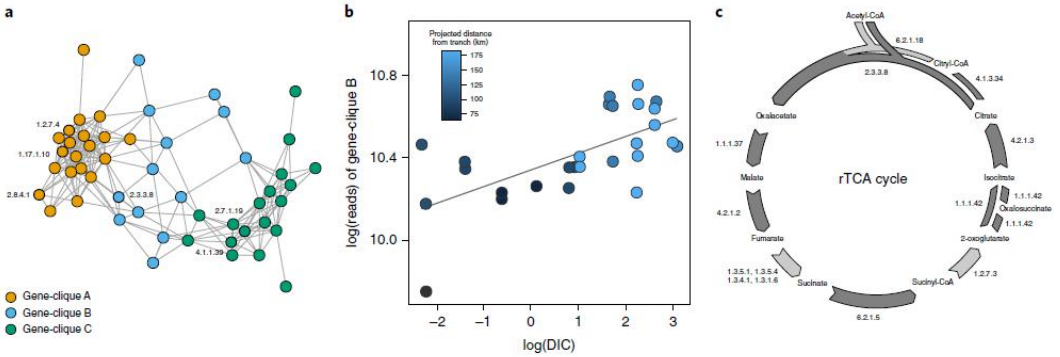

Fig 4. Metagenome-derived genes from the same carbon-fixation pathway correlate with each other and with subduction zone geochemistry. **a**, Co-occurrence network

analysis of the genes involved in all central carbon-metabolism pathways, with edges representing Spearman correlations with a $\rho > 0.5$ ($P < 0.01$, $n = 49$, Holm-corrected). The key genes for the major carbon-fixation pathways were recovered in discrete gene cliques: Wood – Ljungdahl key genes in gene-clique A, rTCA genes in gene-clique B and Calvin – Benson – Bassham in gene-clique C. The key genes for each pathway are highlighted with thicker outlines and have the Enzyme Commission (EC) number plotted. **b**, Sum of gene-clique B genes (normalized read abundance for each enzyme) plotted against DIC concentrations (in mmolC l^{-1}) with blue colour saturation corresponding to the distance from the trench (in km) for each site (Spearman correlation of $\rho = 0.66$; $P < 0.001$, $n = 27$, Holm-corrected). **c**, Diagram of the rTCA cycle with genes recovered in gene-clique B highlighted in dark grey. These include the key genes ATP citrate (pro-S) lyase and the citryl-CoA lyase necessary for the functioning of the two alternative versions of the rTCA cycle[33]. The two light grey rTCA genes were present in the samples but did not correlate as tightly with the other genes to be included in gene-clique B, suggesting they were also used in other pathways. EC numbers are shown.

3. 堆晶橄榄石：重稀土元素成矿的新宿主

翻译人：冯婉仪 fengwy@sustech.edu.cn

Brandt S, Fassbender M L, Klemd R, et al. ***Cumulate olivine: A novel host for heavy rare earth element mineralization [J]****. Geology, 2021, 49: 457-462.*
https://doi.org/10.1130/G48417.1

摘要：橄榄石是恢复岩浆作用过程的重要矿物之一，但对火成岩和矿床中富铁橄榄石的稀土元素（REE）体系了解甚少。通过原位激光剥蚀-电感耦合等离子质谱法（LA-ICP-MS）分析发现，来自布什维尔德大火成岩省（LIP）的古元古代 Vergenoeg F-Fe-REE 矿床中的堆晶铁橄榄石（Fe_2SiO_4）具有有史以来被报道的橄榄石中最高的重稀土元素（HREE）含量，其中 HREE 的浓度高达 6000 倍球粒陨石的 HREE 浓度值。原子探针断层扫描图证实 HREE 进入到铁橄榄石的晶格中，这与锂作为主要的电荷平衡剂以及与布什维尔德 LIP 有关的高分异长英质母熔体中高的 REE 含量密切相关。铁橄榄石的高重稀土含量及其高模态丰度（>95 vol%）表明铁橄榄石堆晶体是 Vergenoeg 矿床 HREE 成矿的主要宿主。Vergeneeg 矿床中的铁橄榄石表明富铁橄榄石可以使大量的 HREE 发生分馏，并且铁橄榄石堆晶体是未来 HREE 勘探的潜在目标。

ABSTRACT: Olivine is one of the most important minerals used to reconstruct magmatic processes, yet the rare earth element (REE) systematics of Fe-rich olivine in igneous rocks and ore deposits is poorly understood. As detected by in situ laser ablation–inductively coupled plasma–mass spectrometry (LA-ICP-MS) analysis, cumulate fayalite (Fe_2SiO_4) in the Paleoproterozoic Vergenoeg F-Fe-REE deposit of the Bushveld large igneous province (LIP) in South Africa contains the highest heavy REE (HREE) contents ever recorded for olivine, with HREE enrichment of as much as 6000× chondritic values. Atom probe tomography maps confirm the incorporation of the HREEs into the fayalite crystal lattice, facilitated by lithium acting as a main charge balancer and by high REE contents in the highly fractionated felsic parental melt that

is related to the Bushveld LIP. The high HREE concentrations of fayalite in concert with its high modal abundance (>95 vol%) indicate that the fayalite cumulates are the main host for the HREE mineralization of the Vergenoeg deposit. Fayalites of Vergenoeg demonstrate that Fe-rich olivine may fractionate large amounts of HREEs, and we propose fayalite cumulates as potential future targets for HREE exploration.

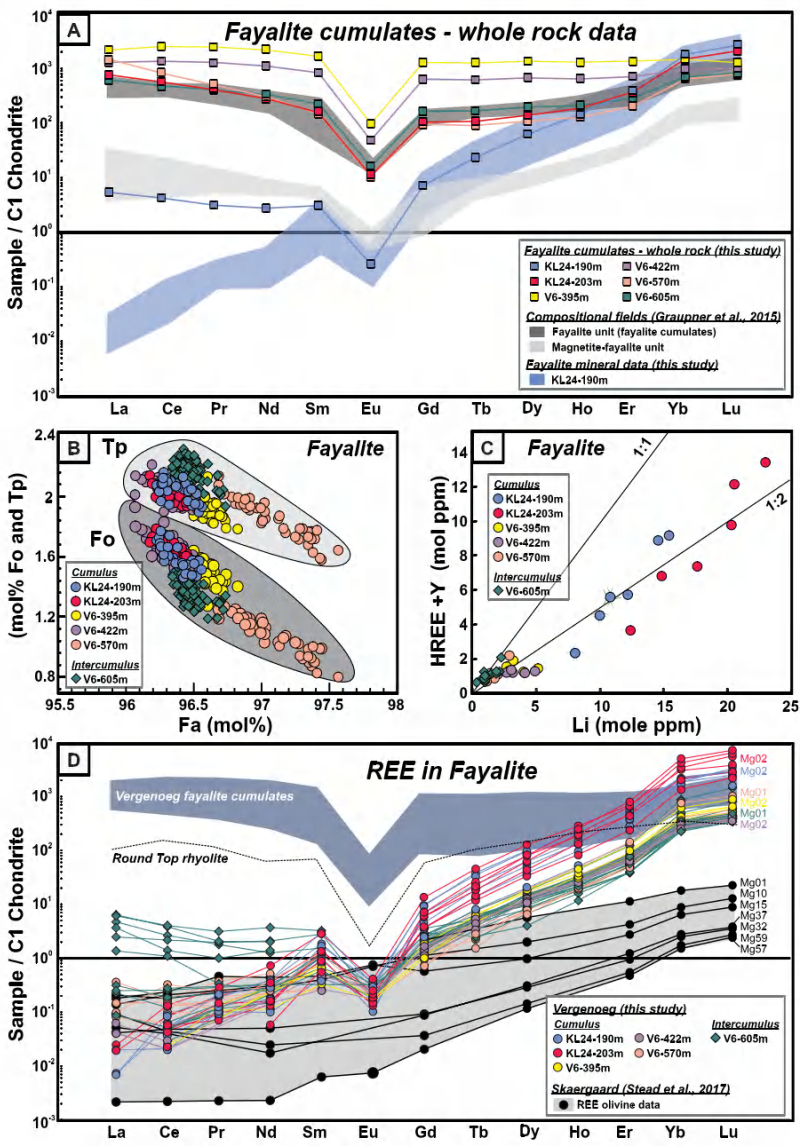

Fig1. (A) Chondrite-normalized rare earth element (REE) patterns for Vergenoeg (South Africa) fayalite cumulates and fayalite of sample KL24-190 m. Also shown are compositional fields for the fayalite and magnetite-fayalite units (Graupner et al., 2015). (B) Correlation of Fe (fayalite, Fa), Mg forsterite, Fo), and Mn (tephroite, Tp) endmembers of olivine. (C) Correlation of Y + heavy rare earth elements (HREEs) and Li in fayalite. (D) Chondrite-normalized REE patterns of fayalite from Vergenoeg, and olivine of the Skaergaard layered intrusion (East Greenland) (Stead et al., 2017). Also shown are the REE pattern of the Vergenoeg fayalite cumulates (from A) and of the rhyolites of Round Top HREE deposit (Texas, USA) (Jowitt et al., 2017). Normalization factors in A and D are from McDonough and Sun (1995).

4. 北大西洋冰川东部边界流对冰盖-AMOC 相互作用和气候变化的重要驱动作用

翻译人:李园洁 liyj3@sustech.edu.cn

Toucanne S, Soulet G, Riveiros N V, et al. ***The North Atlantic Glacial Eastern Boundary Current as a key driver for ice-sheet-AMOC interactions and climate instability [J]****. Paleoceanography and Paleoclimatology, 2021: e2020PA004068. https://doi.org/10.1029/2020PA004068*

摘要：大西洋经向翻转环流（AMOC）的上支对大洋环流和气候变化具有重要作用，但是其在末次冰期的变化记录较少。本文，作者研究北大西洋的向北流动的冰川东部边界流(GEBC)，今天称为欧洲大陆坡流，代表着 AMOC 上支的最东部分。基于流速和同位素的记录，作者展示了~50-15 ka 期间 Dansgaard-Oeschger (D-O) 间冰期 (冰期) 对应更快 (更弱) GEBC。类比现代条件，这表明 D-O 间冰期 (冰期) 期间亚极涡旋及北部水生产力和 AMOC 强度增强 (减弱)。~30-17 ka 期间 GEBC 和欧洲冰盖具有同步振荡表明 AMOC 在向极地运输热量和淡水到北大西洋北部的过程中 AMOC 上支的积极作用，并对深层水的形成和 AMOC 强度具有直接影响。作者揭示了冰盖-AMOC 相互作用和末次冰期及间冰期气候的突然变化。

ABSTRACT：The upper branch of the Atlantic meridional overturning circulation (AMOC) plays a critical role in ocean circulation and climate change, yet its variability during the last glacial period is poorly documented. Here, we investigate the northward-flowing Glacial Eastern Boundary Current (GEBC) in the North Atlantic, known today as the European Slope Current, and representing the easternmost portion of the upper branch of the AMOC. Based on flow speed and isotopic records, we show that Dansgaard-Oeschger (D-O) interstadials (stadials) correspond to a faster (weaker) GEBC during the ~50-15 ka period. This, by analogy to present-day conditions, suggests enhanced (reduced) strength of the subpolar gyre and, by extension, of

northern-sourced water production and AMOC during D-O interstadials (stadials). Concomitant fluctuations of both the GEBC and the European Ice Sheet between ~30 and 17 ka suggest an active role of the upper branch of AMOC in the poleward transport of heat and freshwater to the northern North Atlantic, with direct impacts on deep water formation and AMOC strength. We explore these ice-sheet-AMOC interactions and the associated abrupt climate changes over the last glacial period and the last deglaciation.

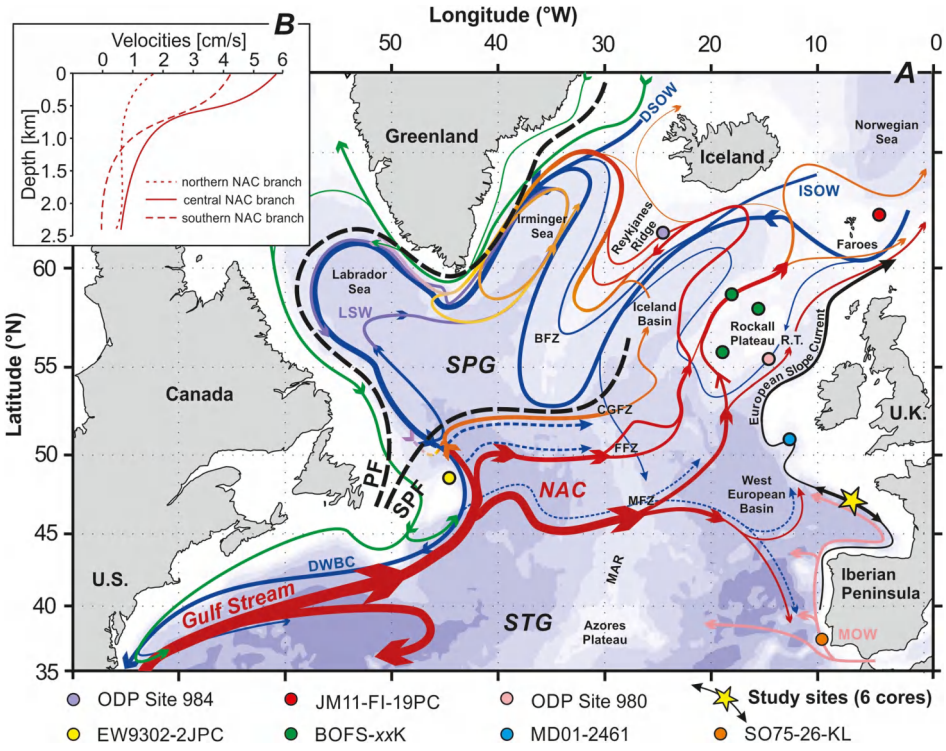

Fig 1. The modern North Atlantic Ocean circulation. (a) Detailed schematic of the upper cell of the AMOC with a warm, northward flow in the upper Atlantic (Gulf-Stream—North Atlantic Current (NAC) system, upper branch of the AMOC; red arrows), the formation of North Atlantic Deep Water (NADW) at high latitudes (i.e., DSOW, ISOW, and LSW; see below), and southward return flow (lower branch of the AMOC; blue arrows) at depth (including the Deep Western Boundary Current, DWBC). The main water masses are indicated: Denmark Strait Overflow Water (DSOW), Iceland-Scotland Overflow Water (ISOW), Labrador Sea Water (LSW) and Mediterranean Outflow Water (MOW). Dashed blue arrows highlight eastward recirculation of NADW by interior pathways. The European Slope Current (~500–2,000 m along the European margin, black arrow), the Greenland currents (in green) and the polar (PF) and subpolar (SPF) fronts (dashed black lines) are shown. SPG: subpolar gyre. STG: subtropical gyre. The main topographical features controlling the flow pathways are labeled: Bight Fracture Zone (BFZ), Charlie–Gibbs Fracture Zone (CGFZ), Faraday Fracture Zone (FFZ), Maxwell Fracture Zone (MFZ), Mid-Atlantic Ridge (MAR), and Rockall Trough (RT). Color changes in the bathymetry at 100 m, at 1,000 m, and every 1,000 m below 1,000 m. Colored circles show the location of the core sites/records discussed in this study, including those from the French Atlantic margin (yellow star; Figure S1)

(adapted from Daniault et al., 2016). (b) Averaged velocity (cm/s) profiles for the NAC branches (Daniault et al., 2016).

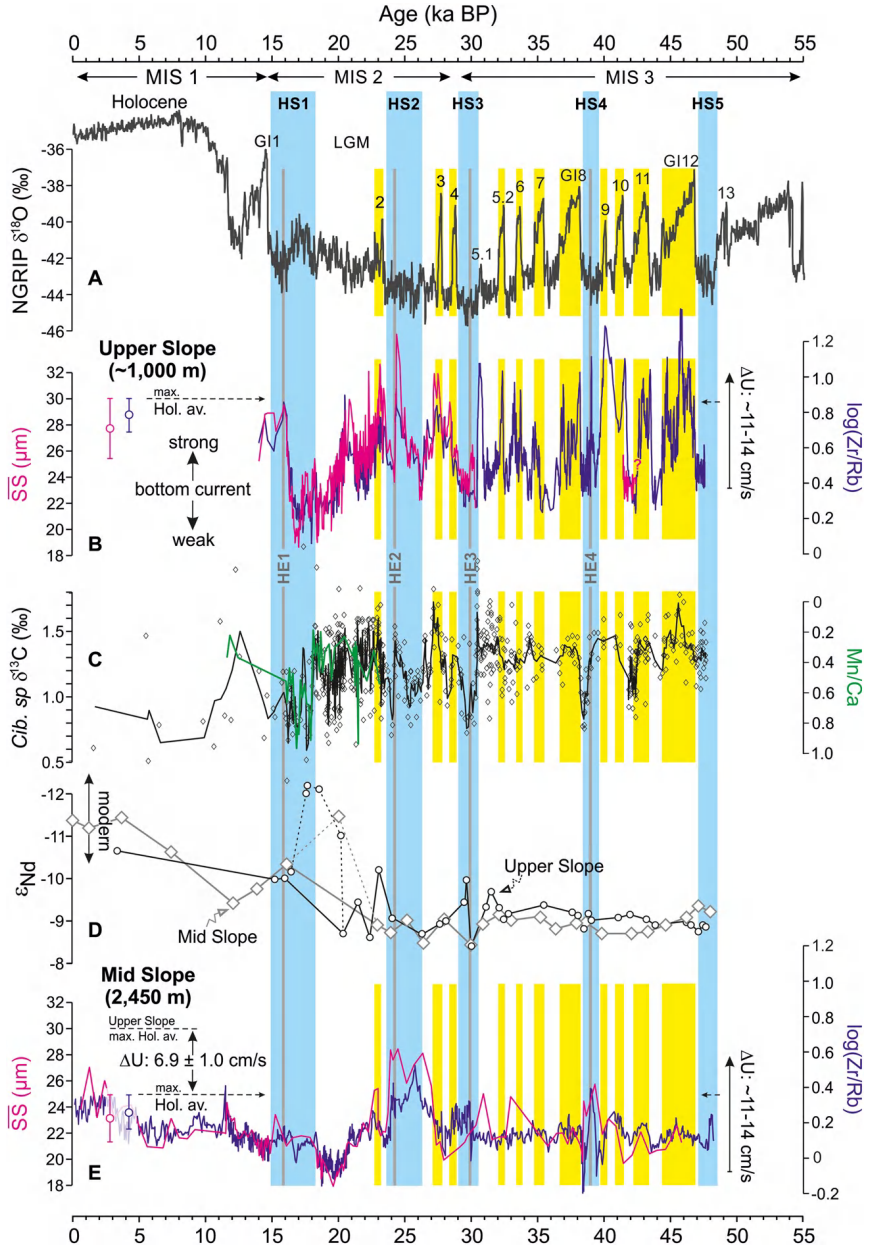

Fig 2. Reconstructions of ocean circulation changes on the French Atlantic margin over the last 50,000 years. (a) NGRIP $\delta^{18}O$ (GICC05 chronology; Rasmussen et al., 2006, 2014; Svensson et al., 2008). (b) Near-bottom flow speed (U) on the upper slope (~1,000 m) reconstructed from SS (magenta line, three-point running average) and XRF log (Zr/Rb) (blue lines; three- and ten-point running average for the 30–0 and 48–30 ka intervals, respectively) composite records. Note that only the SS(and associated XRF Zr/Rb) data "validated" by McCave & Andrews' (2019) recommendation are shown (see Section 5.1). The few "validated" data for the Holocene are shown through

averages (see Table S4 for details). MIS 3 data are from core BOB-CS03. (c) Benthic $\delta^{13}C$ composite record from the upper slope (black line; threepoint running average) and (benthic) foraminiferal Mn/Ca from core MD99-2328 (green line; Mojtahid et al., 2017). These data reflect the variability of bottom water ventilation (Figure S8). (d) Uncleaned foraminifera εNd records from the upper ("stacked" data from BOB-CS03 and BOB-CS05; black line) and middepth cores (MD04-2842; gray line) (Table S6). The modern range of εNd in the Bay of Biscay (0–3,000 m; Figure S9) is indicated (Copard et al., 2011; Dubois-Dauphin et al., 2017). Local inputs of European Ice Sheet sediment-laden meltwater likely explains the unradiogenic εNd values at ~20–17 ka (see Section 6.3 for details). (e) Near-bottom flow speed (U) on the middepth slope (2,450 m) reconstructed from SS (magenta line) and XRF Zr/Rb (blue line; three-point running average) data from core MD04-2842. Yellow bands: Greenland Interstadials (GI). Gray bands: Heinrich Events (HE). Light blue bands: Heinrich Stadials (HS). See Figures S3 and S4 for their definition in the local stratigraphic records. MIS: Marine Isotope Stage.

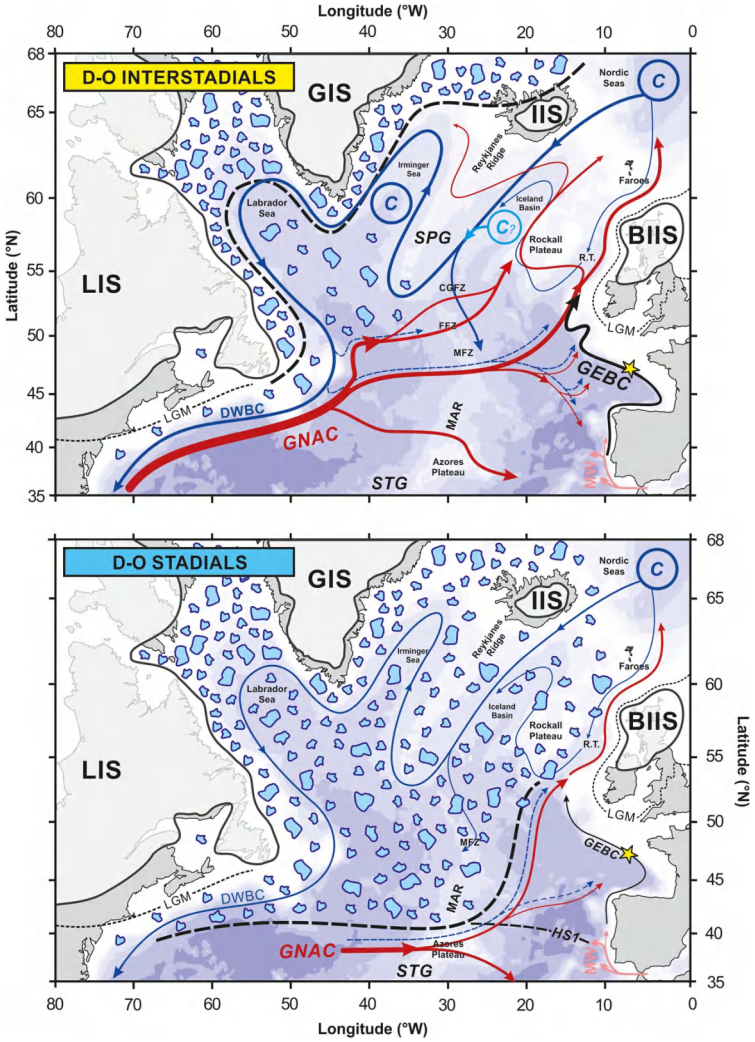

Fig3. Schematic of the North Atlantic circulation during D-O interstadials (upper panel) and stadials (lower panel) of MIS 3. The red and blue continuous arrows indicate the NAC (as the main portion of the upper branch of the AMOC) and the southward return flow (lower branch) of AMOC, respectively. The Glacial Eastern Boundary Current (GEBC), that is a glacial version of the modern European Slope Current, is shown (black arrows). The black dashed lines show plausible scenarios for winter sea ice extent (15% ice concentration), equivalent to the polar front (Li et al., 2010). The strength of the GEBC is maximal during D-O interstadials. Our hypothesis is that this is due to enhanced production and export of intermediate-deep waters (NSW) in the northern North Atlantic open-ocean convection (C) sites (i.e., stronger strength of the subpolar gyre during D-O interstadials compared to D-O stadials). During D-O stadials, the GNAC would follow the polar front, precluding direct entrance of its main branch into the Bay of Biscay. During D-O interstadials and stadials, the GEBC is largely

recruited from the eastern North Atlantic water masses (including recirculated NSW; dashed blue arrows). SPG: subpolar gyre. STG: subtropical gyre. BIIS: British- Irish Ice Sheet (that is the western part of the European Ice Sheet). IIS, Icelandic Ice Sheet; GIS, Greenland Ice Sheet; LIS, Laurentide Ice Sheet. The labels of the main topographical features are detailed in Figure 1. AMOC, Atlantic meridional overturning circulation; NAC, North Atlantic Current.

5. 下加利福尼亚(28-30° N) San Borja 和 Jaraguay 单成因火山群的综合古地磁研究:有关纬度校正

翻译人：张琪 zhangq7@sustech.edu.cn

Mahgoub A N, Garcia-Amador B I, Alva-Valdivia L M. ***Comprehensive palaeomagnetic study of San Borja and Jaraguay monogenetic volcanic fields, Baja California (28–30°N): considerations on latitudinal corrections [J]****. Geophysical Journal International, 2021, 3, 1897-1919.*

https://doi.org/10.1093/gji/ggab064

摘要：我们报告了从墨西哥西北部南下加利福尼亚半岛的 27 个地点获得的 24 个古地磁方向和 10 个高质量的 Thellier 法获得的古强度值。样品来自于 San Borja 和 Jaraguay 单成因火山群的 4 个岩石单元(镁质安山岩、钙碱性熔岩、闪长岩、埃达克岩)。这些单元的喷发时间在 15-2.6Ma 之间(K-Ar 和 $^{40}Ar/^{39}Ar$ 数据)，因此，结果按中新世中晚期和上新世两个连续时期呈现。采样点中已确定的主要磁性矿物为钛磁铁矿、磁铁矿和少量赤铁矿，粒度大小不一，以互生或围岩形式存在，反映了高温岩浆喷涌过程中不同的氧化/还原条件。根据以往的地质和地球物理记录，仔细考虑了该区域的运动演化，使得每个采样点的古方位得以独立还原。还对以前的古方位进行了评估，并对构造运动进行了修正，以便与目前的数据相结合。据此，从总共 74 个数据点中选取 15 个和 36 个方向数据分别用来计算上新世和中晚期的古方位。上新世(Plat=87.8°，Plong=147.5°，K=41.06，A95=6.0°)，中晚中新世(Plat=86.0°，Plong=172.7°，K=41.08，A95=3.8°)，经过构造修正后计算出的古极点位置与预期的北美参考极点无统计学差异。中新世中晚期虚拟地磁极点的构造修正在将结果倾斜度从 2.7°降低到-0.8°方向发挥了重要作用。上新世和中新世中晚期的古强度平均值分别为 29.2±9.1 和 23.2±6.3 μT。整合全球经过滤的古强度数据，结合我们的结果，表明中新世中晚期地磁场强度较上新世（$6.4\pm2.8\times10^{22}$ Am^2）弱（虚拟偶极矩=$5.0\pm2.2\times10^{22}$ Am^2），与现今值相当（7.6×10^{22} Am^2）。这表明中新世中晚期的低偶极矩具有全球性。

然而，与古强度数据时空分布有关的问题仍然是验证这些建议的障碍，因此，仍然需要更多更为可靠的数据。

ABSTRACT: We report 24 palaeomagnetic directions and 10 high-quality Thellier-derived palaeointensity (PI) values, obtained from 27 sites located in Baja California Peninsula, northwestern Mexico. Sampling was done in four rock units (magnesian andesites, calc-alkaline lavas, ignimbrites, adakites) belonging to San Borja and Jaraguay monogenetic volcanic fields. These units have erupted between ~15 and 2.6 Ma (previous K-Ar and 40Ar/39Ar data); hence results are presented in two consecutive periods: middle-late Miocene and Pliocene. The identified main magnetic minerals in the sampled sites are titanomagnetite, magnetite and minor hematite, of variable grain size, present as intergrowths or surrounding grains, which reflect varying oxidation/reduction conditions during emplacement of high-temperature magmas. Based on previous geological and geophysical records, the kinematic evolution was carefully considered in the region, allowing for the independent restoration of the palaeoposition of each sampled site. Previous palaeodirections were also evaluated and corrected for tectonic motion in order to combine them with present data. Accordingly, a number of 15 and 36 directional data are used to calculate palaeopole position for Pliocene and middle-late Miocene periods, respectively, selected from a total of 74 data points. Pliocene (Plat = 87.8°, Plong = 147.5°, K = 41.06, A95 = 6.0°) and middle-late Miocene (Plat = 86.0°, Plong = 172.7°, K = 41.08, A95 = 3.8°) palaeopole positions, calculated after tectonic corrections, are not statistically different from expected North American reference pole. Tectonic correction for Middle-late Miocene virtual geomagnetic poles plays an important role in reducing the resultant tilting from 2.7° to –0.8°. PI mean were calculated for Pliocene and middle-late Miocene periods at 29.2 ± 9.1 and 23.2 ± 6.3 μT, respectively. Compiling global filtered PI data, together with our results, indicates that the strength of the geomagnetic field during middle-late Miocene was weak (virtual dipole moment = 5.0 ± 2.2 × 10^{22} Am^2) compared to Pliocene (6.4 ± 2.8 × 10^{22} Am^2), and also relative to the present-day value (7.6 × 10^{22} Am^2). This indicates the global nature of the low dipole moment during the middle-late Miocene

period. However, issues related to the spatio-temporal distribution of PI data still present an obstacle to validating these suggestions; therefore, more reliable data are still needed.

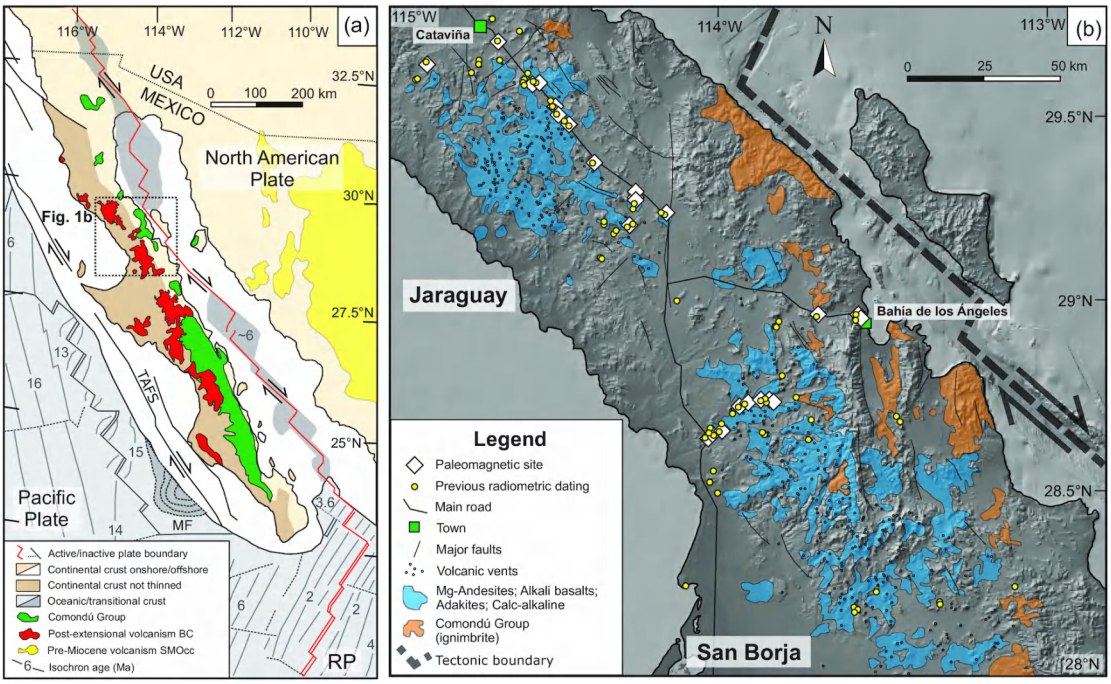

Fig1. (a) Geological map representing the main volcanic fields and geology of Baja California, as well as the distribution of the main tectonic structures (Modified from Aguillón-Robles et al. 2001; Calmus et al. 2003; Pallares et al. 2007; Fletcher et al. 2007). (b) Location of the sampling sites (white diamonds) carried out in the monogenetic volcanic fields of San Borja and Jaraguay, as well as the distribution of outcrops of magnesian andesites (light blue). Sampling was designed so as to drilled in the same coordinates of the previous radiometric data (yellow circles, Table S1), or within a 10-m circumference.

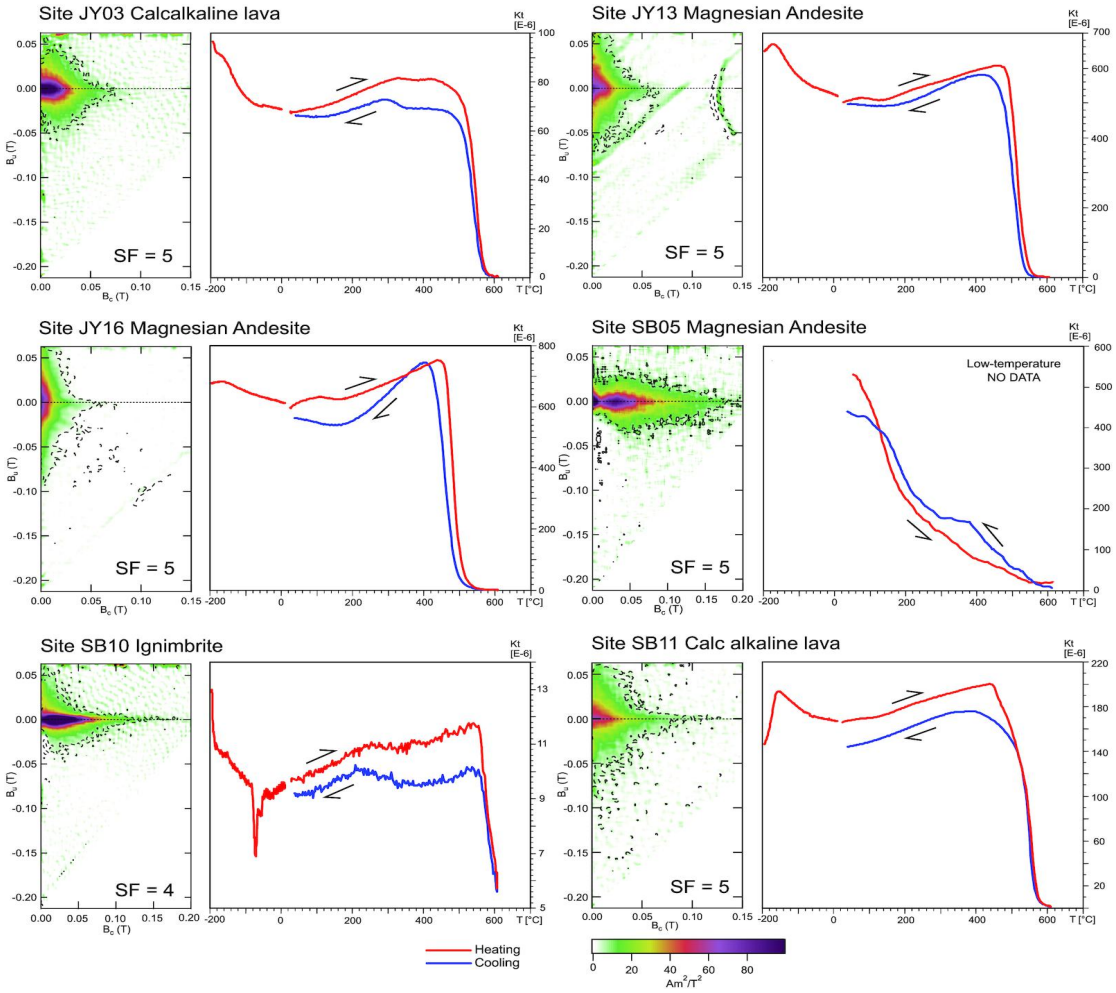

Fig2. Plot of first order reversal curves diagrams and thermomagnetic curves (susceptibility versus temperature) for representative samples from San Borja (SB) and Jaraguay (JY). SF: smoothing factor.

6. 东亚热带地区在过去 60ka 的季节性干旱事件

翻译人：杨会会 11849590@mail.sustech.edu.cn

Zhang J P, Lu H Y, Jia J W, et al. ***Seasonal drought events in tropical East Asia over the last 60,000y [J]****. Proceedings of the National Academy of Sciences, 2020, 117(49):30988–30992.*

https://doi.org/ 10.1073/pnas.2013802117

摘要: 末次冰期期间的冰阶-间冰阶东亚热带地区季节性水文变化的原因仍存在争议。本文通过植硅体和孢粉记录发现了 7 个发生在相对温暖的间冰阶的季节性干旱事件。这些事件明显表现为高比例的二齿植硅体，并与热带太平洋西部至东部的大尺度纬向海温梯度相一致，这表明热带太平洋纬向海温梯度的变化和北半球 Hadley 环流的变化导致了西太平洋副热带高压的西移，可能是导致季节降水减少的主要原因。我们的发现强调了纬向和经向海气环流，而不是仅仅热带辐合带或 ENSO 振荡，控制了末次冰期热带东亚的水文变化。

ABSTRACT: The cause of seasonal hydrologic changes in tropical East Asia during interstadial/stadial oscillations of the last glaciation remains controversial. Here, we show seven seasonal drought events that occurred during the relatively warm interstadials by phytolith and pollen records. These events are significantly manifested as high percentages of bilobate phytoliths and are consistent with the large zonal sea-surface temperature (SST) gradient from the western to eastern tropical Pacific, suggesting that the reduction in seasonal precipitation could be interpreted by westward shifts of the western Pacific subtropical high triggered by changes of zonal SST gradient over the tropical Pacific and Hadley circulation in the Northern Hemisphere. Our findings highlight that both zonal and meridional ocean–atmosphere circulations, rather than solely the Intertropical Convergence Zone or El Niño-Southern Oscillation, controlled the hydrologic changes in tropical East Asia during the last glaciation.

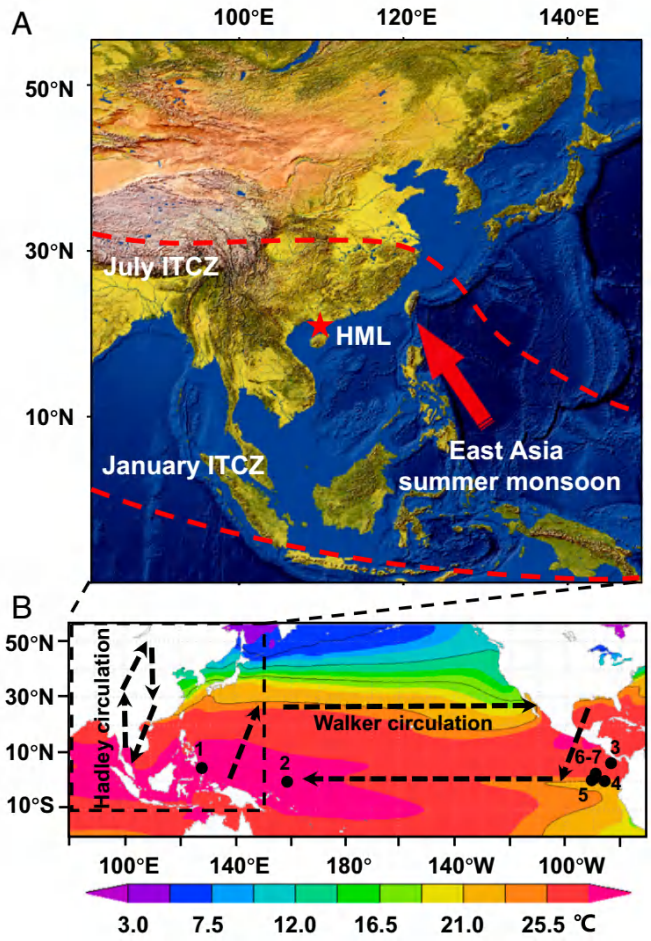

Fig1. Geographical and climatological settings of study site and region. (A) Topographic map from ENVI 5.1 showing the location of study site (red star, Huguangyan Maar Lake, HML) in south China and seasonal positions of ITCZ (30). (B) Schematic map showing the settings of atmospheric circulations and SSTs in the tropical Pacific. Black solid circles indicate cores mentioned in this paper: 1 = MD98-2181, 2 = ODP806B, 3 = MD02-2529, 4 = ME0005A-24JC, 5 = ODP846, 6 = TR163-22, and 7 = TR163-19. Colors are annual mean SSTs from the period 1981–2010 obtained from https://psl.noaa.gov.

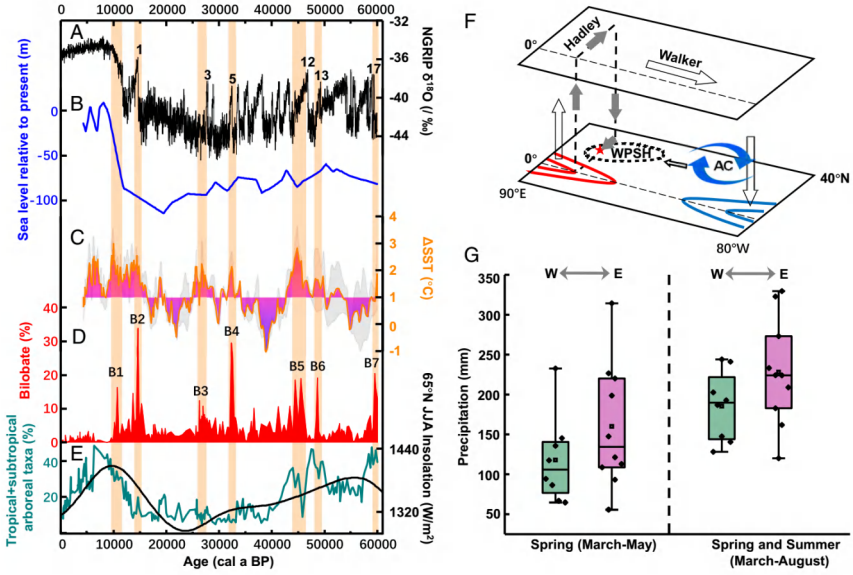

Fig2. Comparison of multiproxy data from the HML core with regional and global climatic records over the past 60 ka, schematic diagram showing circulation anomalies, and regional rainfalls associated with these circulation anomalies. (A) $\delta^{18}O$ record from NGRIP (on a GICC05 timescale) (45–48), numbers indicate D/O events; (B) global sea-level changes (49); (C) ΔSST of the western (12, 38) and eastern (39) tropical Pacific; gray indicates the SD of ΔSST; (D) percentage of bilobates from HML, B1-B7 indicate seven bilobate events; (E) pollen percentage of tropical and subtropical arboreal taxa from HML together with 65°N summer insolation (June, July, and August, JJA) (black line); (F) schematic diagram showing circulation anomalies with positive and negative heating (red and blue curves) in the western and eastern tropical Pacific, respectively; "AC" indicates anticyclonic circulation; (G) modern precipitation recorded by the Zhanjiang Meteorological Station in the years when the WPSH moves to the westernmost (green bar, W) and easternmost (pink bar, E) locations during spring and spring–summer. We defined the center of the WPSH by the average 588 dagpm (101geopotential meter) at 500 hPa; the westward shift years are 1980, 1983, 1988, 1991, 1996, 1998, 2003, and 2010, and the eastward shift years are 1984, 1985, 1986, 1992, 1994, 1997, 1999, 2000, 2002, and 2004 (50). The meteorological data are from the China Meteorological Data Service Center (http://data.cma.cn).

7. 南海东部次海盆海底扩张过程中洋壳结构和岩浆作用随时间的变化

翻译人：刘伟 inewway@163.com

Yu J, Yan P, Qiu Y. ***Oceanic crustal structures and temporal variations of magmatic budget during seafloor spreading in the East Sub-basin of the South China Sea [J]****. Marine Geology, 2021: 106475.*

https://doi.org/10.1016/j.margeo.2021.106475

摘要：在贫岩浆型大陆裂谷作用之后，南海在~33 - ~15 Ma 之间发生海底扩张，并于~25 Ma 发生了向南的洋脊跃迁，形成了东部次海盆、西北次海盆和西南次盆地。然而，由于缺乏洋壳结构成像，在扩张期间的岩浆过程仍然鲜为人知。本文展示了从东部次海盆从北边洋陆过渡带(COT)到残留扩散脊的三条地震剖面，以揭示地壳结构。在北部，洋壳厚度仅为 3.9-4.5 km，基底起伏，断层众多，莫霍反射面较弱，指示了岩浆作用相对较少，从岩浆贫乏的大陆裂谷作用到最初的扩张，构造伸展持续时间较长。从 COT 北部到洋脊跃迁处，基底变得平滑，断层相对平滑，莫霍反射面趋于连续和强烈，洋壳逐渐变厚(局部厚度达 8.4 km)，表明这一扩张时期（33-25 Ma）岩浆作用显著增加。而从洋脊跃迁处至残留扩张脊处，洋壳基底又因断裂作用而变得起伏，地壳逐渐变薄，在残留扩张脊只有 3.7 km，且可看到一个深谷，指示了这段海底扩张时期(25- 15 Ma)岩浆活动减少，构造扩张增加。因此，东部次海盆洋壳结构的变化反映了扩张过程中岩浆作用由增到减的显著变化，峰值出现在洋脊跃迁前后。薄的构造地壳和残留扩张脊附近的深谷进一步支持了南海扩张后期缓慢的海底扩张，也表明即使存在海南地幔柱的岩浆贡献，其贡献也可能非常有限。

ABSTRACT: Following magma-poor continental rifting, the South China Sea (SCS) experienced seafloor spreading from ~33 Ma to ~15 Ma with an intervening southward ridge jump at ~25 Ma, generating the oceanic East, Northwest and Southwest Sub-basins. However, the magmatic processes during spreading remain poorly known owing

to the lack of oceanic crustal images. Here we present a composite profile comprising three seismic lines that run from the northern continent-ocean transition (COT) to the extinct spreading center of the East Sub-basin to reveal the crustal structures. In the northernmost oceanic portion, the first oceanic crust featuring rough basement with numerous faults, and diffuse and weak Moho reflector, is only 3.9–4.5 km thick, implying relatively low magmatic budget and protracted tectonic extension continued from the magma-poor continental rifting to initial spreading. From the northern COT ocean-ward to the abandoned ridge where the jump event occurred, the basement becomes smooth with subdued faults. The Moho reflector tends to be continuous and strong, and the igneous crust gradually becomes thick (locally up to 8.4 km), suggesting considerably increasing magmatic budget during the early spreading stage. However, in the central portion spanning from the abandoned ridge to the extinct spreading axis, the basement becomes rough with crustal faults again. And the crust gradually becomes thin, to only 3.7 km at the extinct spreading center where a deep median valley is still visible, though severely altered by post-spreading volcanism, implying decreasing magmatic budget and increasing tectonic extension during the late spreading stage. Therefore, the crustal structure variations in the East Sub-basin reflects a prominent increasing to decreasing change of magmatic budget during spreading with the peak around the intervening ridge jump. Thin, tectonized crust and deep median valley around the extinct spreading center further support slow seafloor spreading during the last spreading stage of the SCS which ended at ~15–16 Ma, and also suggest that magma contribution from the Hainan mantle plume might be very limited if any.

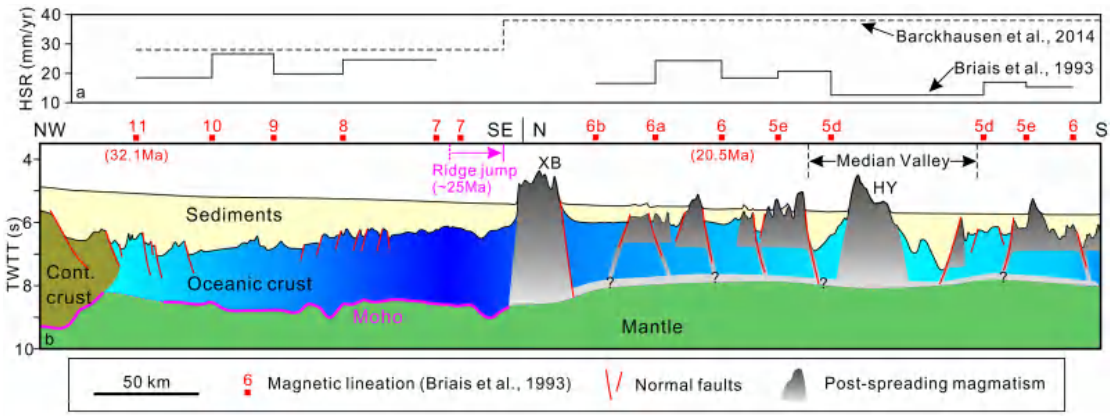

Fig1. Half spreading rate (HSR) (a) and schematic interpretation of oceanic crustal structures (b) in the ESB along a composite profile combined by MCS lines 1555, East-1 and 97301. The solid black lines in (a) represent the HSRs calculated from the magnetic lineations interpreted by Briais et al. (1993) with the spreading cessation at ~15 Ma, while the dashed black lines are the HSRs from Barckhausen et al. (2014) with the spreading cessation at 20.5 Ma. The thick carmine lines in (b) indicate the reflection Moho imaged in MCS lines 1555 and East-1. The dashed and solid vertical carmine lines in (b) mark the locations of the abandoned spreading ridges before and after jump at ~25 Ma, respectively. The zone from the abandoned ridge to the extinct spreading center were altered and thickened by post-spreading magmatic intrusions and extrusions. Even so, the median valley is still visible from the basement morphology. HY: Huangyan Seamount; XB: Xianbei Seamount.

8. 中国直升机时域电磁技术进展

翻译人：曹伟 11930854@qq.com

Jun Lin, Jian Chen, Fei Liu, and Yang Zhang. ***The Helicopter Time-Domain Electromagnetic Technology Advances in China [J]****. Surveys in Geophysics, 2021(42):585-624.*

https://doi.org/10.1007/s10712-021-09635-7

摘要：直升机时域电磁法(HTEM)是利用地球物理勘探技术和直升机平台搭载电磁探测设备的一种方法。近几年来，HTEM 技术以其效率高、覆盖地形陡峭多变、探测深度大、分辨率高等优点，在理论和技术上都取得了迅速的发展。本文简要介绍了 HTEM 的技术原理和正反演理论，总结了国际上具有代表性的 HTEM 系统的主要性能参数，对比了 VTEM、SkyTEM 和 HeliTEM 系统的性能和结构特点。为了向从事 HTEM 仪器技术的学者提供技术参考，本文分析了影响 HTEM 系统探测能力的因素以及系统设计中的主要难点。以我国 HTEM 系统为分析对象，详细介绍了系统集成的关键技术，包括大功率发射、接收传感器设计和运动噪声抑制技术。本文还讨论了 HTEM 技术的发展趋势和存在的技术问题，包括探测深度、测量精度、噪声细化分类等，为今后 HTEM 技术的进一步发展提供了思路。

ABSTRACT: The helicopter time-domain electromagnetic (HTEM) method is a method that uses geophysical exploration technology and a helicopter platform to carry electromagnetic detection equipment. HTEM has developed rapidly, in both theoretical and technological terms, in recent years because of its high efficiency, ability to drape steep and variable terrain, large detection depth, and high resolution. This work briefly introduces the HTEM technology principle and forward and inversion theory, summarizes the main performance parameters of international representative HTEM systems, and analyzes the performance and structural characteristics of VTEM, SkyTEM and HeliTEM systems. To provide a technical reference for scholars engaged

in HTEM instrument technology, we analyze the factors affecting the detection capability of HTEM systems and the main difficulties in system design. Taking China s HTEM systems as the object of analysis, we introduce the key technologies behind the systems in detail, including high-power transmitting, receiving sensor design, and motion-noise-suppression technologies. This work also discusses the development trend of HTEM and the existing technical problems, including detection depth, measurement accuracy, and noise refinement classification, providing ideas for the further development of HTEM technology in the future.

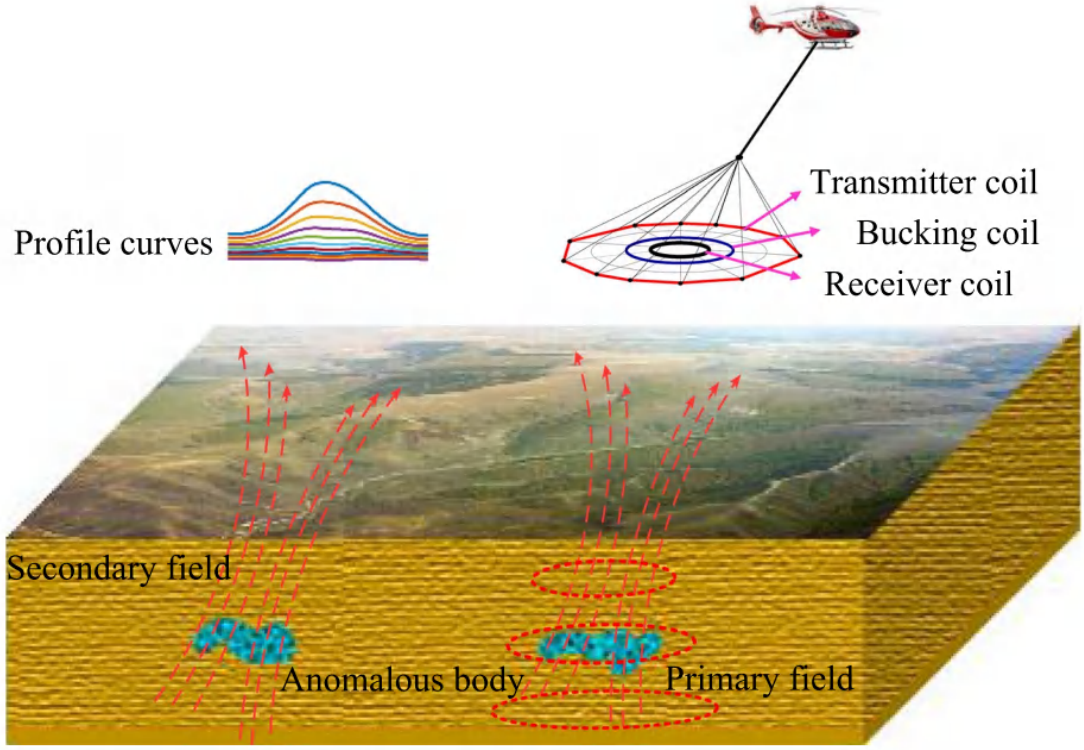

Fig 1. Schematic of HTEM method.

9. 始新世以来夏威夷岛链移动的新证据

翻译人：王敦繁 dunfan_w@foxmail.com

Parés J M, Moore T C. ***New evidence for the Hawaiian hotspot plume motion since the Eocene [J]****. Earth and Planetary Science Letters, 2005, 237 (3–4):951-959. https://doi: 10.1016/j.epsl.2005.06.012*

摘要：海底一堆厚厚的生物化石沉积物，反映了赤道地区的高生物生产力，可以用来确定太平洋岩石圈板块的纬向运动。基于赤道相的纬向运动估算的板块运动独立于古地磁数据和热点轨迹，因此可以进一步检验运动学模型。我们根据赤道沉积相所显示的古赤道位置，确定了近 53 万年太平洋板块的北移。对 26～69 个 DSDP 和 ODP 站点的热带太平洋地区过去 53 个百万年最高沉积速率区域进行了取样。根据这些地点的堆积速率图，我们不仅可以确定古赤道的位置，而且可以估算出早始新世以来的赤道大圆和自旋轴的相对位置。从夏威夷链海山相对于夏威夷热点的纬度变化推断出的太平洋板块向北运动始终高于从赤道沉积相分析推断出的。这种差异是夏威夷热点在过去 53 个百万年的一次纬向转移造成的。总的来说，我们在底特律、仁德和科科海山的观察和最近的古地磁结果与晚白垩世以来夏威夷地幔柱向南运动一致。研究结果表明，夏威夷热点在过去的 4300 万年中以每年~32 毫米的速度向东南方移动，而太平洋板块自 53 Ma 以来以每年 25 毫米的平均速度向北移动~128 毫米。

ABSTRACT: A thick mound of fossiliferous sediments, reflecting high biogenic productivity at the Equator can be used to determine latitudinal motion of the Pacific lithospheric plate. Plate motion estimates based on the latitudinal movement of Equatorial facies are independent of paleomagnetic data and hotspot tracks and thus permit further testing of kinematic models. We have determined the northward motion of the Pacific Plate for the last 53 Myr based on the position of the paleoequator as shown by Equatorial sediment facies. Between 26 and 69 DSDP and ODP Sites sample the past 53 Myr in the tropical Pacific. Based on the mapped patterns of accumulation

rates in these sites, we were able not only to determine the position of the paleoequator but also to estimate the Equatorial great circle and hence the relative position of the spin axis since the early Eocene. The northward motion of the Pacific Plate inferred from the change in latitude of dated Hawaiian Chain seamounts relative to the Hawaiian hotspot is consistently higher than that deduced from the analyses of Equatorial sediment facies. Such a difference results from a latitudinal shift of the Hawaiian hotspot during the last 53 Myr. All together, our observations and recent paleomagnetic results from the Detroit, Nintoku and Koko seamounts [J.A. Tarduno, R.A. Duncan, D.W. Scholl, R.D. Cottrell, B., Steinberger, T. Thordarson, B.C. Kerr, C.R. Neal, F.A. Frey, M. Torii, M., C. Carvallo. The Emperor Seamounts: Southward motion of the Hawaiian hotspot plume in Earth's mantle. Science 301 (2003) 1064–1069.] are consistent with a progressive southward motion of the Hawaiian mantle plume since the Late Cretaceous. Our results suggest that the Hawaiian hotspot moved at ~32 mm/yr to the SE during the past 43 million years and that the Pacific Plate moved ~128 northward since 53 Ma at an average rate of 25 mm/yr.

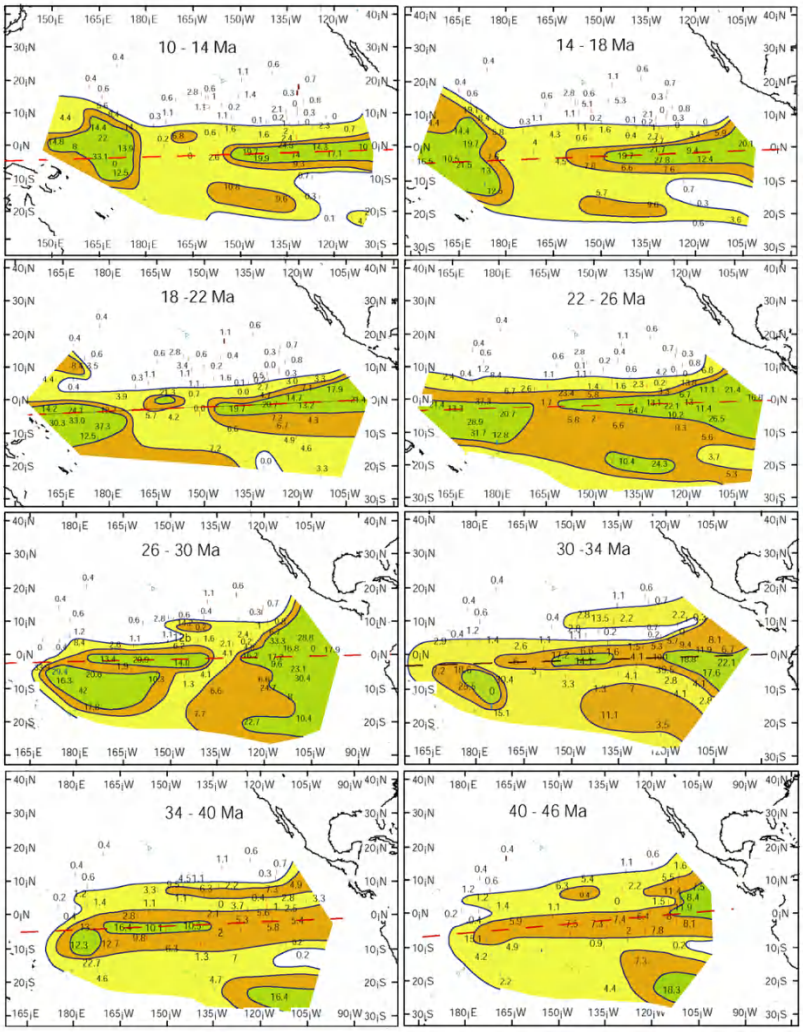

Fig1. Maps of sediment accumulation rates in the equatorial Pacific averaged over 4 to 6 m.y. using DSDP and ODP Sites on the Pacific lithospheric plate (after Moore et al.), see reference for details of site rotations and stratigraphy used). The dashed line in each map indicates estimated position of the paleoequator based on a fit by eye to pass through the center of the tongue of higher accumulation rates. Accumulation rates for each time interval at each site are shown in units of m/m.y. beside site locations. Shaded contour intervals at 1 m/ m.y., 5 m/m.y. and 10 m/m.y.

10. 在空间变化的岩浆流中晶体的旋转和排列

翻译人：张伟杰 12031188@mail.sustech.edu.cn

Vachon R, Bazargan M. ***Crystal rotations and alignment in spatially varying magma flows: 2-D examples of common subvolcanic flow geometries [J]****. Geophysical Journal International. 2021, 266(1):709-727.*

https://doi.org/10.1093/gji/ggab127

摘要：粘性流体携带的细长颗粒的旋转速率通常与流动的局部角速度不同。通常，颗粒会形成一种净排列，所得到的颗粒集合的形状优势取向可用于应变标记，以重建流体的速度场。前人对流动导致颗粒旋转动力学的研究主要集中于空间均匀流，主要应用于大规模构造变形。最近，这一理论被扩展到空间变化的流动，如携带晶体的岩浆通过火山管道移动。此外，还引入了晶体取向概率密度函数的演化方程。本文,我们把这个新理论应用到几个岩浆入侵常见简单二维流几何图形,如从岩墙流入储库或从储库流入岩墙、在一个膨胀或收缩型储库里流动、在突然转弯的岩墙内流动、岩浆房内热对流。其主要目的是为解释野外观测和建立更复杂的携带晶体流动模型提供指导。我们发现，携带晶体的长宽比越大，晶体排列的相干性越强，而对排列图形的几何形状影响较小。由于自然系统中晶体旋转方程的各种扰动，我们证明了在理想系统中发现的时间周期行为在自然界中可能是短暂的，并且晶体排列可以用时间平均解很好地描述。我们也证实了一些早期的发现。例如，在通道壁附近，流体流动通常沿着边界面，由此产生的简单剪切流导致近似平行于边界的首选晶体方向。当纯剪切变形占主导时，晶体有向最大拉伸应变速率方向定向的趋势。当流动撞击边界时，例如在一个膨胀的岩浆房或作为热对流模式的一部分，纯剪切的拉伸成分与边界对齐，晶体就会向这个方向定向。在野外，这种局部模式可能很难与边界平行的简单剪切流区分开来。收缩岩浆房纯剪切也控制着晶体沿岩浆房的壁面，在岩浆流偏离岩浆库壁面的地方首选的晶体方向与壁面垂直。总的来说，我们发现我们计算出的晶体取向图样与类似几何形状的模拟实验结果吻合得很好。

ABSTRACT: Elongate inclusions immersed in a viscous fluid generally rotate at a rate that is different from the local angular velocity of the flow. Often, a net alignment of the inclusions develops, and the resulting shape preferred orientation of the particle ensemble can then be used as a strain marker that allows reconstruction of the fluid's velocity field. Much of the previous work on the dynamics of flow-induced particle rotations has focused on spatially homogeneous flows with large-scale tectonic deformations as the main application. Recently, the theory has been extended to spatially varying flows, such as magma with embedded crystals moving through a volcanic plumbing system. Additionally, an evolution equation has been introduced for the probability density function of crystal orientations. Here, we apply this new theory to a number of simple, 2-D flow geometries commonly encountered in magmatic intrusions, such as flow from a dyke into a reservoir or from a reservoir into a dyke, flow inside an inflating or deflating reservoir, flow in a dyke with a sharp bend, and thermal convection in a magma chamber. The main purpose is to provide a guide for interpreting field observations and for setting up more complex flow models with embedded crystals. As a general rule, we find that a larger aspect ratio of the embedded crystals causes a more coherent alignment of the crystals, while it has only a minor effect on the geometry of the alignment pattern. Due to various perturbations in the crystal rotation equations that are expected in natural systems, we show that the time-periodic behaviour found in idealized systems is probably short-lived in nature, and the crystal alignment is well described by the time-averaged solution. We also confirm some earlier findings. For example, near channel walls, fluid flow often follows the bounding surface and the resulting simple shear flow causes preferred crystal orientations that are approximately parallel to the boundary. Where pure shear deformation dominates, there is a tendency for crystals to orient themselves in the direction of the greatest tensile strain rate. Where flow impinges on a boundary, for example in an inflating magma chamber or as part of a thermal convection pattern, the stretching component of pure shear aligns with the boundary, and the crystals orient themselves in that direction. In the field, this local pattern may be difficult to distinguish from a boundary-parallel simple shear flow. Pure shear also dominates along the walls

of a deflating magma chamber and in places where the flow turns away from the reservoir walls, but in these locations, the preferred crystal orientation is perpendicular to the wall. Overall, we find that our calculated patterns of crystal orientations agree well with results from analogue experiments where similar geometries are available.

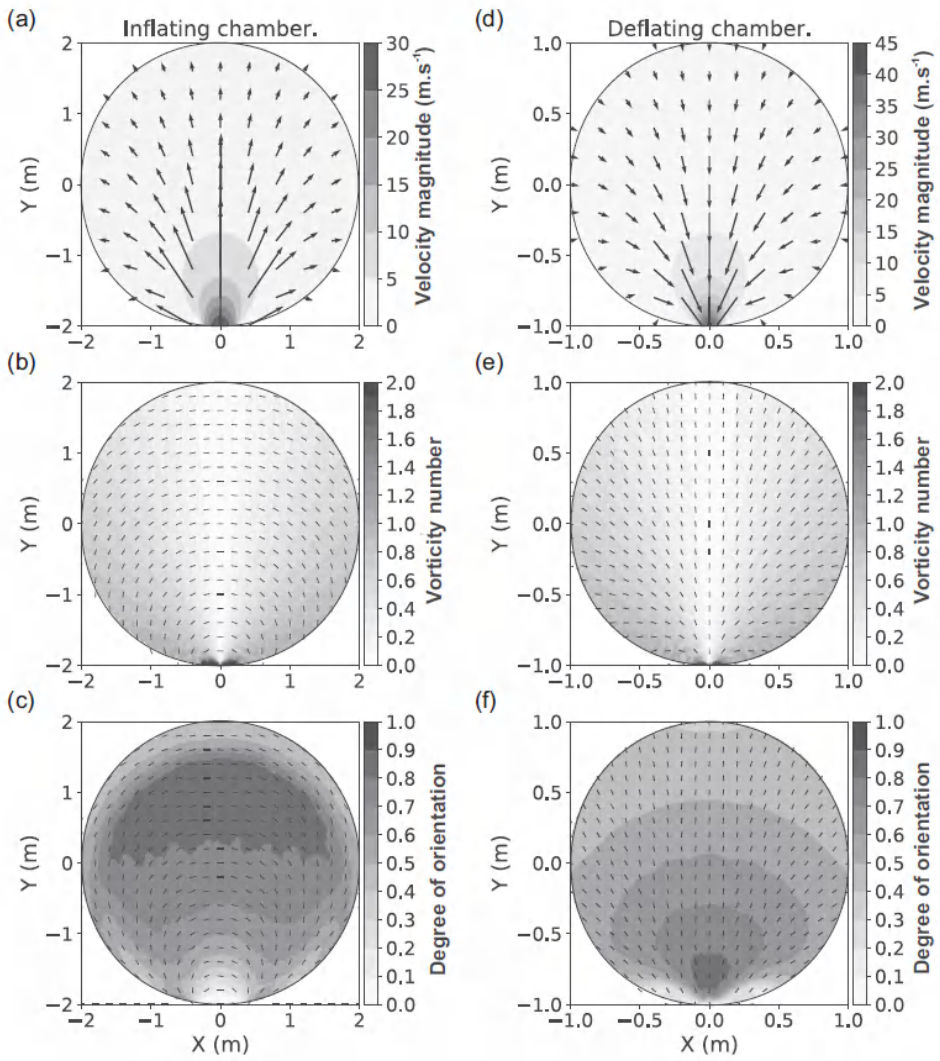

Fig1. Results for the models of inflation and deflation of a magma reservoir. Fluid enters or exits the model domain via an inlet or outlet located at the bottom of the reservoir. (a) and (d) Velocity magnitude (shading) and direction (arrows) of the fluid flow. (b) and (e) Vorticity number (shading) and orientation of ε̇1 (tick marks). (c) and (f) Degree of orientation of the PDF (shading) and most likely orientation (peak of PDF) of particles with aspect ratio a/b = 2 (tick marks). In the inflation model, particles mostly

align perpendicular to the flow, while in the deflation model, particles align with the flow.

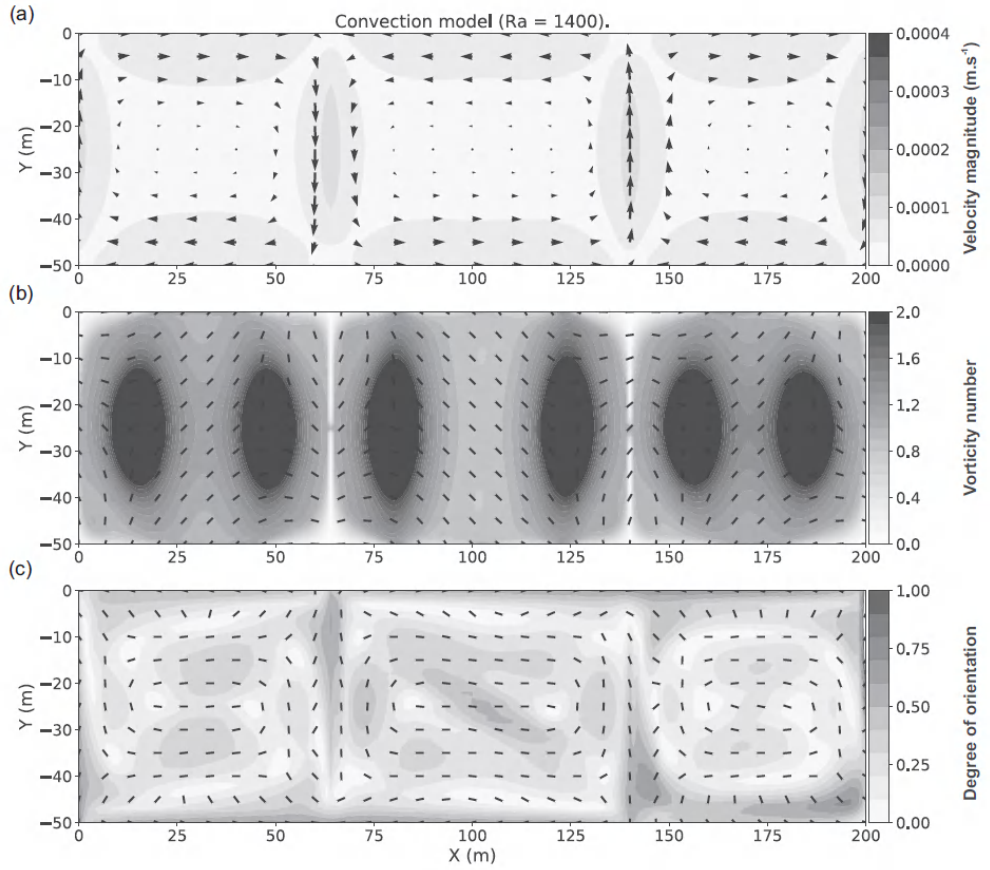

Fig2. Results for thermal convection with Rayleigh number of 1400. (a) Velocity magnitude (shading) and direction (arrows) of the fluid flow. (b) Vorticity number (shading) and orientation of ˙ε1 (tick marks). (c) Degree of orientation of the PDF (shading) and most likely orientation (peak of PDF) of particles with aspect ratio a/b = 2 (tick marks).

11. 非洲东南部 2500 cal BP 以来的古地磁记录

翻译人：李海 12031330@mail.sustech.edu.cn

Haberzettl T, Kasper T, Stoner J S, et al. ***Extending and refining the paleomagnetic secular variation database for south-eastern Africa (Madagascar) to 2500 cal BP [J].*** *Earth and Planetary Science Letters. 2021, 565, 116931.*

https://doi.org/10.1016/j.epsl.2021.116931

摘要：现今对非洲南部的古地磁长期变化的了解较少。作者从马达加斯加的 3 个小火山口沉积物中获得古地磁记录，Andraikiba 和 Amparihibe 分别位于马达加斯加主岛和西北部一个小岛上的陆地玛珥湖，而 Crater Lake 是一个与印度洋的玛珥湖。通过研究样品的交变退磁结果，发现 2500 年以来的（除了最近 400 cal BP）两个沉积记录的特征剩磁方向具有相似的变化模式。这些新数据可检验以前那些低分辨率和受其他因素影响的数据的可靠性。这将为从受到干扰的数据中提取研究区可靠的古地磁记录提供可能。虽然 La Réunion, South Africa, Botswana 和 Zimbabwe 的古地磁数据分辨率较低且记录时间间隔较短，但这些数据表现出较好的连续性。尽管在年代上存在偏差，但仍与全球地磁模型 SHAWQ2K 较为相似。此外，磁偏角的变化还与 CALS3K.4 模型的变化趋势相似。与之相反的，从 Malawi 湖的沉积记录中没有发现相似的磁偏角变化，但磁倾角的变化具有较强的一致性。在研究区以北 5000 公里的 Makran 也记录相似的磁倾角变化。有趣的是，显示这些倾角相似性的记录的空间分布与模型预测中检测到倾角异常的空间分布相似。PSV 在如此大范围内的相似性指示了一个有别于非偶极子场西向漂移的大规模岩浆动力成因。这项研究强调了马达加斯加的玛珥湖在古地磁重建中的潜力，在扩充非洲古地磁数据库时，应尽可能避免浅海系统。

ABSTRACT: Today's knowledge about paleomagnetic secular variations in (southern) Africa is extremely limited. Here, we derive paleomagnetic records from independently radiocarbon dated sediment records from three maars in Madagascar: Andraikiba and Amparihibe are terrestrial maars located on the main island of Madagascar and on a

small island in the Northwest, whereas Crater Lake is a maar which has an open connection to the Indian Ocean. Studied through alternating field demagnetization of u-channel samples, characteristic remanent magnetization (ChRM) directions document similar inclination and declination patterns in two of the archives for the past 2,500 years (except for the last 400 cal BP). These new data are the first allowing to test the reliability of previous records which often suffer from low resolution and other obstacles. This will further allow to start to distinguish between robustly confirmed paleomagnetic secular variation data for this region from potentially problematic data. Considering a much lower resolution and a shorter covered time interval of archaeomagnetic data from La Réunion, South Africa, Botswana and Zimbabwe the temporal successions of maxima and minima reveal a coherent picture. Although slightly shifted in time, similarities also exist to the global geomagnetic field reconstruction model SHAWQ2k (Campuzano et al., 2019) which includes the above mentioned data. Surprisingly also similarities, though only in declination, are observed to the CALS3K.4 model (Korte and Constable, 2011) which is used as Northern Hemisphere biased model example. In contrast to this, no declination similarities but remarkable inclination similarities are observed to a lake record from Lake Malawi. An analog inclination pattern is also observed in a record from the Makran Accretionary Wedge which is ~5,000 km to the north of the investigated sites. Interestingly the spatial distribution of archives showing these inclination similarities resembles the spatial distribution of inclination anomalies detected in model predictions. PSV similarities over such a large area are suggestive of a large-scale core dynamic origin independent of westward drift of non-dipole field components often associated with PSV records. This study emphasizes the potential of maar lakes in Madagascar for paleo reconstructions but also suggests that shallow marine and marine-brackish systems should be avoided if possible when trying to expand the (South) African paleomagnetic database.

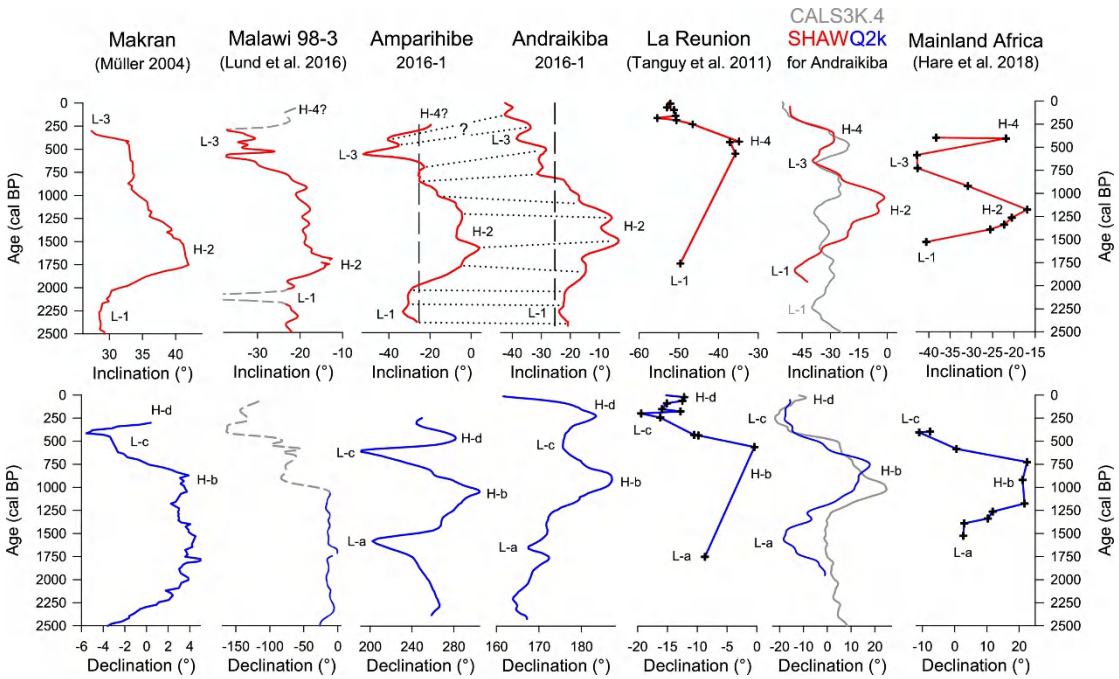

Fig1. Comparison of the measured records (note that declination data are relative since the azimuth could not be controlled during coring) from Andraikiba 2016-1 and Amparihibe 2016-1 (center) plotted on their individual age scale to archaeomagnetic records (right) from La Réunion (Tanguy et al., 2011) as well as mainland southern Africa (i.e., South Africa, Botswana and Zimbabwe (Hare et al., 2018; Neukirch et al., 2012; Tarduno et al., 2015) reduced to the coordinates of Mapungubwe (22.212° S, 29.387° E) (Hare et al., 2018)). Comparisons are also made to the CALS3k.4 (gray) (Korte and Constable, 2011) and SHAWQ2k (red/blue) (Campuzano et al., 2019) models as well as to the Lake Malawi record (Lund et al., 2016), which is the most reliable (Di Chiara, 2020) and closest sedimentary record to our sites and the varve-dated Makran Accretionary Wedge record (Müller, 2004) (both left). Large scale similarities are highlighted by highs (H-) and lows (L-). More detailed similarities between the inclination records of Andraikiba 2016-1 and Amparihibe 2016-1 are highlighted by dotted black lines. Dashed gray lines in the Malawi record indicate data which were not included in the original publication due to potential coring artifacts such as for example twisting during the coring process (Lund et al., 2016).

12. 太平洋深水冲刷和冰消期大气 CO_2 浓度的上升

翻译人：张亚南 zhangyn3@mail.sustech.edu.cn

Jianghui Du, Haley B A, Mix C, et al. ***Flushing of the Deep Pacific Ocean and the Deglacial Rise of Atmospheric CO_2 Concentrations[J]****. Nature Geoscience, 2018, 11, 749-755.*

https://doi.org/10.1038/s41561-018-0205-6.

摘要：在末次冰消期期间（19,000-9,000 年前），大气 CO_2 增加了 80ppm。了解这种变化的内在机制是古气候学的核心话题，也与未来全球变暖过程中 CO_2 转移的预测有关。作者在文中展示了北太平洋沉积物钻孔高分辨率的自生 Nd 同位素，并推断太平洋深海翻转流在末次冰盛期（LGM）减缓，但在冰消期 CO_2 上升阶段间歇性的变强。放射性碳证据表明的冰消期相对老的太平洋深水，被重新解释为来自南极附近的此表层水体中 ^{14}C 年龄的增加，与深海冲刷事件中（Flushing events）老碳从深海转移出，CO_2 释放到大气一致。Nd 同位素的证据表明，冰消期太平洋深海环流的增强，对南半球变暖，海冰退缩和平均大洋温度的变化具有重要的影响。推测出的环流变化幅度和太平洋深水冲刷作为重要的，甚至主导的因素，控制着冰消期大气 CO_2 的上升。

ABSTRACT: During the last deglaciation (19,000–9,000 years ago), atmospheric CO_2 increased by about 80 ppm. Understanding the mechanisms responsible for this change is a central theme of palaeoclimatology, relevant for predicting future CO_2 transfers in a warming world. Deglacial CO_2 rise hypothetically tapped an accumulated deep Pacific carbon reservoir, but the processes remain elusive as they are underconstrained by existing tracers. Here we report high-resolution authigenic neodymium isotope data in North Pacific sediment cores and infer abyssal Pacific overturning weaker than today during the Last Glacial Maximum but intermittently stronger during steps of deglacial CO_2 rise. Radiocarbon evidence suggestive of relatively ‘old’ deglacial deep Pacific water is reinterpreted here as an increase in preformed ^{14}C age of subsurface waters

sourced near Antarctica, consistent with movement of aged carbon out of the deep ocean and release of CO_2 to the atmosphere during the abyssal flushing events. The timing of neodymium isotope changes suggests that deglacial acceleration of Pacific abyssal circulation tracked Southern Hemisphere warming, sea-ice retreat and increase of mean ocean temperature. The inferred magnitude of circulation changes is consistent with deep Pacific flushing as a significant, and perhaps dominant, control of the deglacial rise of atmospheric CO_2.

.

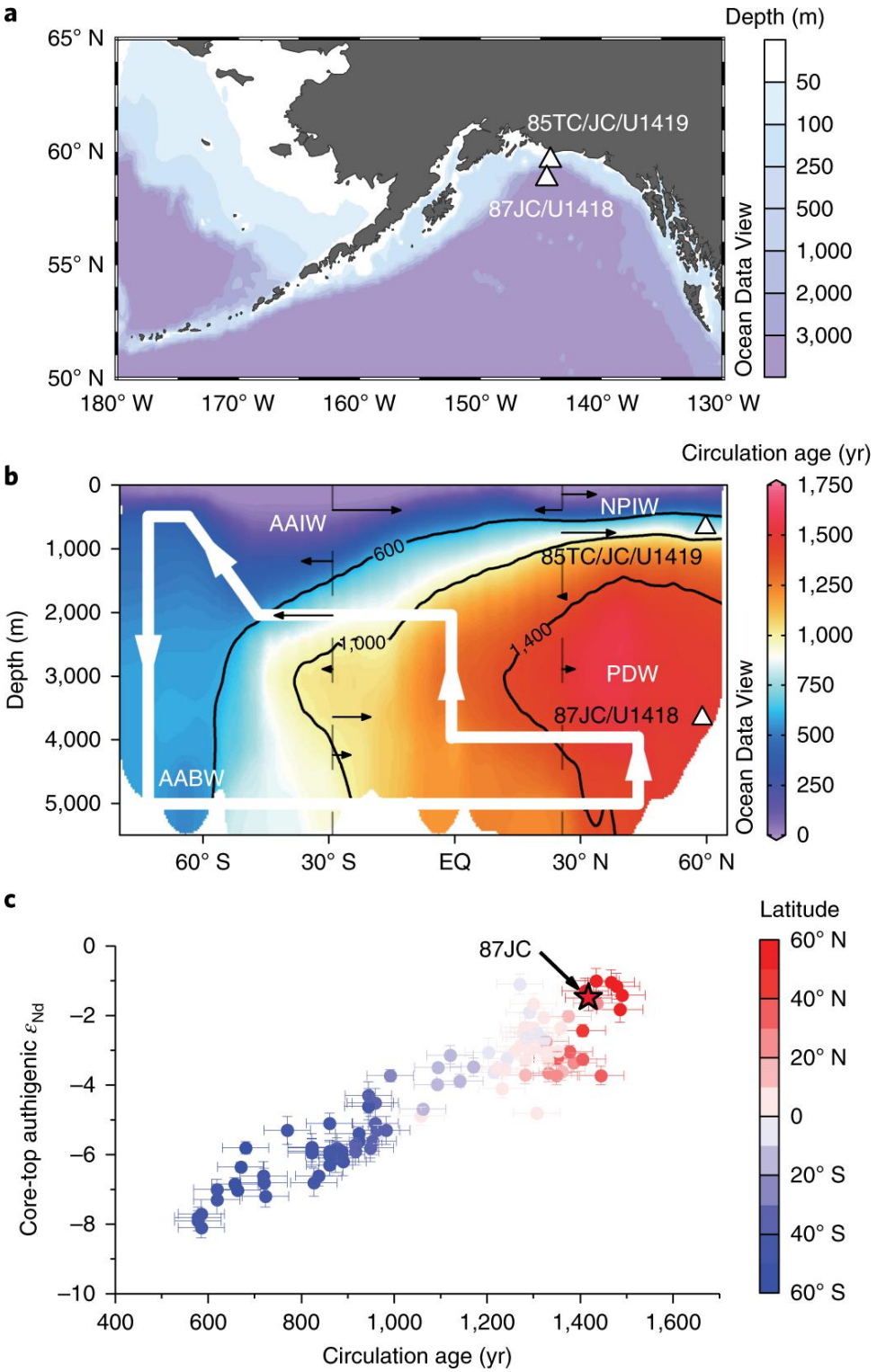

Fig1. Study sites and Pacific circulation. a, Locations of the intermediate-depth and the deep sites in the Gulf of Alaska. b, A meridional (138° W) section of circulation age in the Pacific. Solid small arrows indicate modern water transport across the 28° S and 24° N hydrographic sections and thick arrows show the schematic abyssal circulation. c, Relationship between Pacific core-top authigenic ε_{Nd} (>2,500 m, Supplementary Fig.

2, with 2σ analytical uncertainty) and circulation age (1σ = 50 yr). The star symbol is site EW0408-87JC.

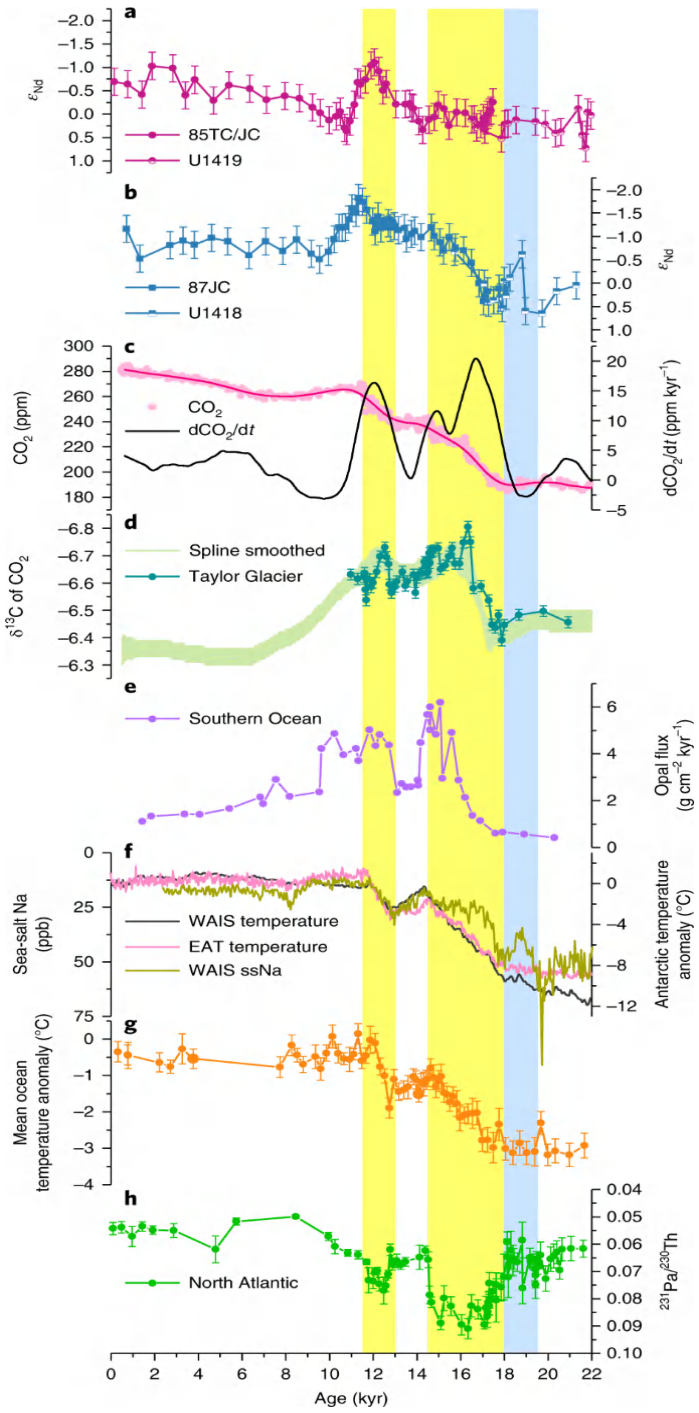

Fig2. Deglacial North Pacific ε_{Nd}, compared with global climate records. a,b, Authigenic ε_{Nd} from site EW0408-85TC/JC/U1419 (a) and site EW0408-87JC/U1418 (b). Error bars in a and b indicate long-term 2σ (0.29ε) external reproducibility. c, Ice-

core CO_2 and its rate of change. d, $\delta^{13}C$ of atmospheric CO_2. e, Southern Ocean opal flux from core TN057-13PC432. f, Temperature anomalies from West (WAIS Divide) and East (EAT) Antarctica, and sea-salt sodium concentration (ssNa, 50-year median value, a proxy for sea ice) from the WAIS Divide. g, Mean ocean temperature anomaly with 1σ uncertainty. h, North Atlantic $^{231}Pa/^{230}Th$ records with 1σ uncertainty. The blue-shaded interval marks the early deglacial increase of temperature and decrease of sea ice in West Antarctica. The yellow-shaded intervals mark the synchronous increase of atmospheric CO_2, decrease of sea ice and increase of temperature in both West and East Antarctica, and rise of global ocean mean temperature.

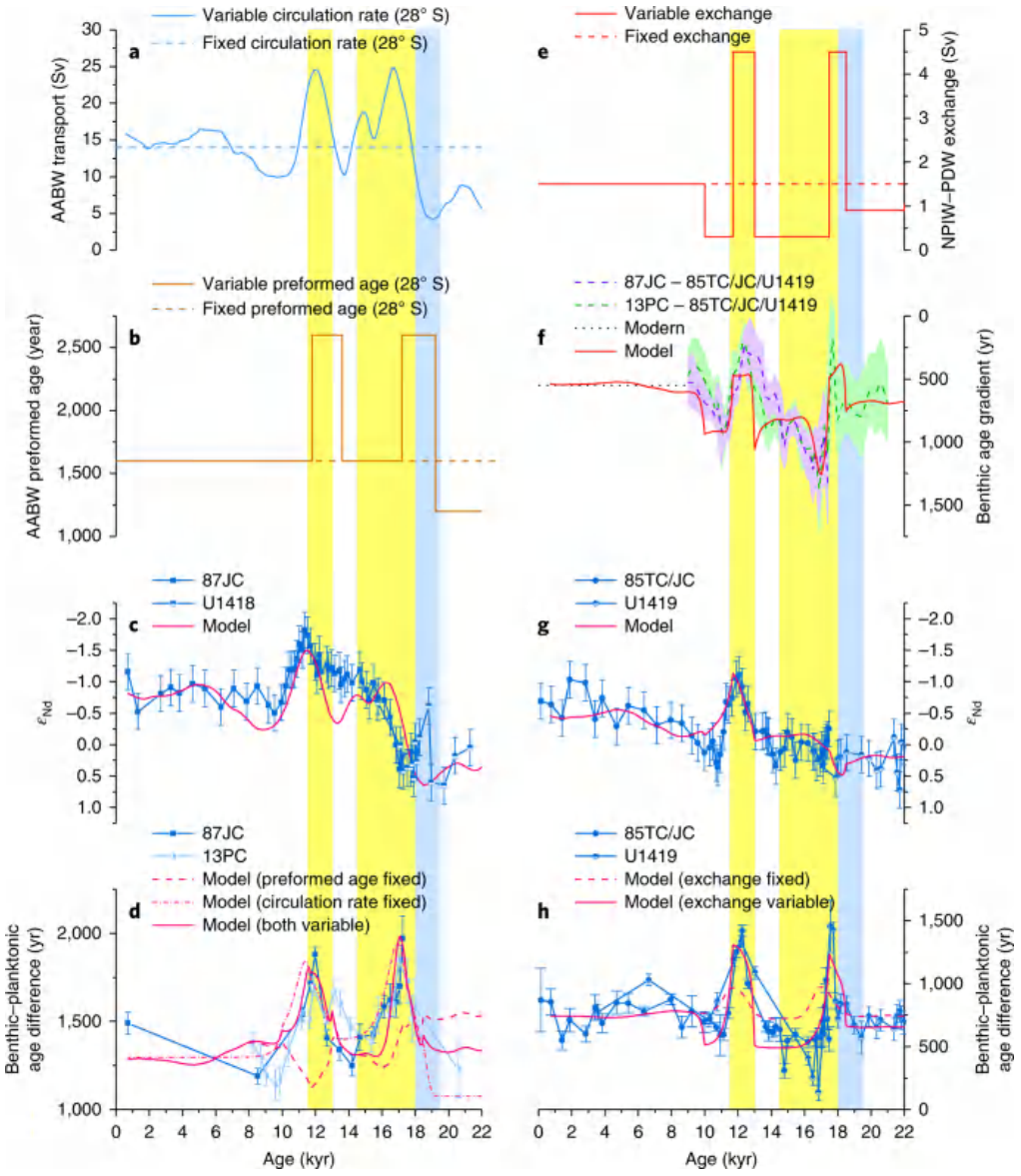

Fig3. Transient simulations of North Pacific circulation tracers. a, AABW transport

scaled to the rate change of atmospheric CO_2. b, The preformed ^{14}C age of AABW. c, Modelled and measured ε_{Nd} at deep site EW0408-87JC/U1418. d, Modelled and measured benthic–planktonic age differences at deep site EW0408-87JC and W8709A-13PC12. Error bars are 1σ analytical uncertainties. e, PDW–NPIW exchange. f, Benthic ^{14}C age gradients between NPIW (EW0408-85TC/JC/U14199) and PDW (EW0408-87JC and W8709A-13PC12) boxes (95% confidence intervals include uncertainties of both age models and ^{14}C measurements), compared with the model output. The dashed line indicates the modern gradient. g,h, The same as c and d respectively but for the intermediate-depth site EW0408-85TC/JC/U1419. The standard simulations are plotted using solid lines. Dashed lines indicate model sensitivity tests. The colour-shaded intervals are the same as in Fig. 2.